

# Mathematical modeling and simulation of coupled aqueous humor flow and temperature distribution in a realistic 3D human eye geometry

Thomas Saigre<sup>1†</sup>, Vincent Chabannes<sup>1</sup>, Christophe Prud'homme<sup>1</sup>, Marcela Szopos<sup>2</sup>,

<sup>1</sup>Institut de Recherche Mathématique Avancée, UMR 7501 Université de Strasbourg et CNRS

<sup>2</sup>Université Paris Cité, CNRS, MAP5, F-75006 Paris, France

<sup>†</sup>Corresponding author: [thomas.saigre@math.unistra.fr](mailto:thomas.saigre@math.unistra.fr)

February 14, 2025

## Abstract

We present a comprehensive computational model to simulate the coupled dynamics of aqueous humor flow and heat transfer in the human eye. To manage the complexity of the model, we make significant efforts in meshing and efficient solution of the discrete problem using high-performance resources. The model accurately describes the dynamics of the aqueous humor in the anterior and posterior chambers and accounts for convective effects due to temperature variations. Results for fluid velocity, pressure, and temperature distribution are in good agreement with existing numerical results in the literature. Furthermore, the effects of postural changes and wall shear stress behavior are analyzed, providing new insights into the mechanical forces acting on ocular tissues. Overall, the present contribution provides a detailed three-dimensional simulation that enhances the understanding of ocular physiology and may contribute to further progress in clinical research and treatment optimization in ophthalmology.

**Keywords :** mathematical and computational ophthalmology, finite element method, thermo-fluid dynamics.

## 1 Introduction

Understanding the behavior of the human eye is challenging, as it involves the study of the interaction between various physical phenomena, such as heat transfer, fluid dynamics, and tissue deformation. The eye is a complex organ in which these phenomena are intricately linked and influence each other in ways that are not yet fully understood. For example, the flow of aqueous humor within the eye can affect intraocular pressure, which in turn can influence the overall health of the tissues. Therefore, it is crucial to develop accurate and efficient computational models to simulate the multi-physics physiology of the ocular system. These models must integrate the various physical processes at play, and capture the interactions between thermal regulation, fluid movements, and mechanical responses of the eye tissues. As a result, researchers can gain a more comprehensive understanding of the underlying mechanisms of ocular physiology, pathology and therapeutic options. Examples in the latter case include hyperthermia for eye tumors [Li+10], cell injection treatment to cure bullous keratopathy [Kin+18], or ocular drug delivery methods [Bha21]. In addition, invasive measurements on human subjects are complex to perform and may result in inaccurate results [RF77]. Therefore, numerical simulations are a valuable tool for investigating the complex interactions between the different physical phenomena in the eye, providing insights that are difficult or even impossible to obtain experimentally.

In the present work, we focus on simulating the flow of the aqueous humor in the anterior and posterior chambers of the human eye and its coupling with the heat transfer inside the eyeball. Previous studies have investigated several aspects of these complex interactions, as reviewed in [Dvo+19]. For instance, [HB02; Wan+16; Mur+23] modeled flow coupled with heat transfer in the anterior chamber (AC) and posterior chamber (PC), while [Sac+23] explored the impact of the intraocular pressure on aqueous humor (AH) flow and drainage. Other works, such as [Can+02; ON08; BBS20; Abd+21; Dvo+22] examined the thermo-fluid dynamics of AH flow in the AC with specified boundary conditions. However, these studies often focused on simplified geometries or did not fully couple the heat transfer within the entire eyeball.

To address these gaps, our work develops a three-dimensional mathematical and computational model that simulates heat transfer throughout the whole human eyeball, coupled with the dynamic flow of AH in both the AC and PC. The present contribution represents an extension of the work presented in [SPS24], where only heat transfer inside the human eyeball was investigated, with a particular focus on the parametric effects. The model aims to provide deeper insights into the thermal environment of the eye and its interaction with fluid dynamics, which is essential for understanding the ocular physiopathology and improving treatment strategies such as drug delivery methods. Special attention is paid to the impact of postural orientation on flow recirculations within the eye. Preliminary results have been presented in [Sai+24a], and we here further extend our analysis and perform a thorough validation process of our findings. Furthermore, the wall shear stress (WSS) generated by the AH flow is an important biomechanical factor,

influencing ocular tissue health and potentially impacting the drainage pathways, which are relevant to conditions such as glaucoma [Yan+22]. We therefore include in our development an original contribution, allowing accurate and efficient computations of the WSS in the anterior and posterior chambers.

Solving the coupled three-dimensional thermo-fluid dynamics model of the eye numerically poses significant computational challenges due to the complexity and nonlinearity of the governing equations. The interaction between heat transfer and fluid flow requires solving large, sparse linear systems that can be computationally expensive and time-consuming. To address these challenges, it is essential to employ adapted preconditioners that can enhance the convergence rate of iterative solvers. By using tailored preconditioning techniques such as GAMG or the Schur complement [ESW14], we achieve faster and more stable solutions, enabling the simulation of more detailed and realistic models of ocular physiology.

The remainder of the article is organized as follows: Section 2 is devoted to the description of the biophysical model of the human eye, focusing on the detailed geometrical representation and the mechanisms governing AH flow. Section 3 presents the discretization techniques and computational framework employed, including the numerical methods and preconditioning strategies used to solve the coupled equations efficiently. Section 4 gathers and discusses the results obtained from our simulations, highlighting the model's capabilities and potential applications. Finally, Section 6 summarizes our findings and outlines future research directions in the field of mathematical and computational ophthalmology.

**Notations:** In this document, the notation  $\vec{v}$  (with an upper arrow) denotes a vector as a physical quantity, while  $\mathbf{v}$  (in boldface) denotes a vector from the algebraic standpoint. In the same spirit  $\underline{\mathbf{A}}$  (underlined) denotes a matrix or a tensor as a physical quantity, while  $\mathbf{A}$  (in boldface) denotes a matrix from the algebraic standpoint.

## 2 Biophysical model

In this section, we present the biophysical model of the human eye that we aim to simulate. We describe the geometrical model of the eye and the biomechanical behavior involved in heat transfer and fluid dynamics.

### 2.1 Geometrical model of the human eye

We denote by  $\Omega$  the domain of the human eye presented in Fig. 1(a). This domain is divided into ten subdomains, representing the different parts of the eye, such as the cornea, the lens, the vitreous body, the retina, *etc.*, with various physical properties. We denote by  $\Omega_{\text{AH}}$  the anterior and posterior chambers of the eye (brown part in Fig. 1(a)), which are filled with the *aqueous humor* (AH), as shown in Fig. 1(b). The geometry, generated from a Computer-Aided Design (CAD) file of a human eye, is based on a realistic human eye model, with dimensions consistent with the average human eye anatomy [Sai24]. All the necessary steps from the CAD description to the mesh are described in [Cha+24], and available in open access [Sai+24b]. Note that (i) the region corresponding to the suspensory ligaments, hatched in Fig. 1(a), is not considered in the model and is included in the vitreous body; (ii) the iris-lens channel, see Fig. 1(b), is really thin [Dvo+18], very difficult to measure accurately and assumed to be in the order of 5 to 10  $\mu\text{m}$ .

### 2.2 Bio-heat and fluid dynamics model

The AH is a transparent fluid produced by the ciliary body that flows from the *posterior chamber* (PC) to the *anterior chamber* (AC), where it is drained through two pathways, the trabecular meshwork, and the uveoscleral pathway, see Fig. 2 for a simplified view. AH flow plays a fundamental role in maintaining the intraocular pressure (IOP) level. In addition to the hydraulic pressure difference created by production and drainage, the AH dynamic is influenced by posture and thermal factors. Specifically, convective effects are produced by the temperature difference between the external environment at the corneal surface and the internal surface, which is at the body temperature.

Following the approach of Abdelhafid et al. [Abd+21] and Wang et al. [Wan+16] (see also [Dvo+19] and references therein for a complete review), we make the following assumptions: (i) The aqueous humor is considered an incompressible Newtonian fluid due to its low compressibility and viscosity. (ii) Density variations in the fluid are small and can be neglected except in the buoyancy term. This approximation, named *Boussinesq approximation*, allows us to model the buoyancy effects due to temperature differences without accounting for full density variations.

Under these assumptions, the steady flow of AH is governed by the incompressible Navier-Stokes equations coupled with heat transfer:

$$\rho(\vec{u} \cdot \nabla)\vec{u} - \nabla \cdot \underline{\underline{\sigma}} = -\rho\beta(T - T_{\text{ref}})\vec{g} \quad \text{in } \Omega_{\text{AH}}, \quad (1a)$$

$$\nabla \cdot \vec{u} = 0 \quad \text{in } \Omega_{\text{AH}}, \quad (1b)$$

$$\rho C_p \vec{u} \cdot \nabla T - k \nabla^2 T = 0 \quad \text{in } \Omega, \quad (1c)$$

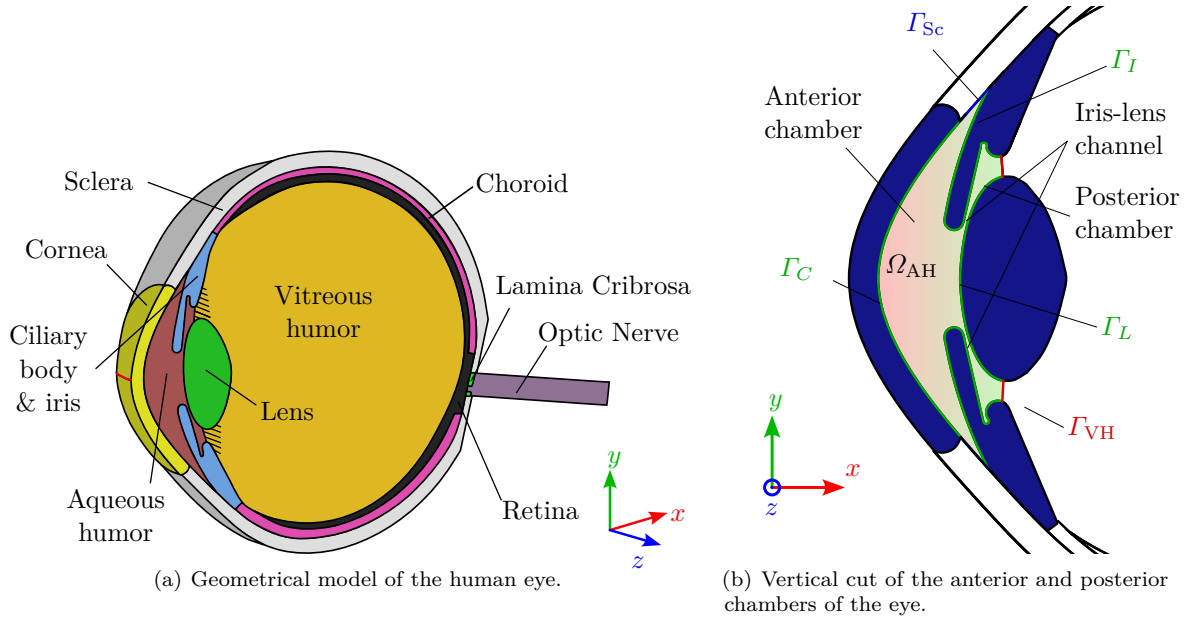


Figure 1: Description of the human eyeball (left panel), zoom on the anterior and posterior chambers of the eye (right panel).

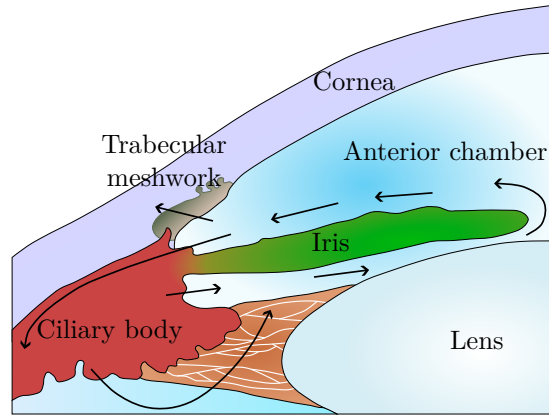


Figure 2: Production and drainage of AH in the front part of the eye, adapted from [RRK13].

where  $\mu$  [N s/m<sup>2</sup>] is the dynamic viscosity of the fluid,  $\rho$  [kg/m<sup>3</sup>] its density (both at reference temperature  $T_{ref}$  [K]),  $C_p$  [J kg<sup>-1</sup> K<sup>-1</sup>] its specific heat,  $k$  [W m<sup>-1</sup> K<sup>-1</sup>] its thermal conductivity. Note that  $k$  is discontinuous piecewise constant function because of the different materials in the eye. We refer to [Sai24, Chap. 1] for more details. The quantity  $T$  [K] is the temperature of the eye, while  $p$  [Pa] is the pressure of the aqueous humor fluid (also expressed in mmHg in a biologic context), and  $\vec{u}$  [m s<sup>-1</sup>] is its velocity. The behavior of the fluid is characterized by the Cauchy stress tensor  $\underline{\underline{\sigma}}$  defined as

$$\underline{\underline{\sigma}}(\vec{u}, p) = -p\underline{\underline{I}} + 2\mu\underline{\underline{D}}(\vec{u}), \quad (2)$$

where  $\underline{\underline{I}}$  is the identity tensor, and  $\underline{\underline{D}}(\vec{u}) = \frac{1}{2}(\nabla\vec{u} + \nabla\vec{u}^T)$  is the *strain rate tensor*. Following [Can+02; NO06], we neglect the metabolic heat generation in the eye due to blood perfusion as there is no literature data available on this topic. However, such a term could be added in further analysis to enhance the model's accuracy.

The right-hand side term in Eq. (1a) represents the gravitational force per unit volume, along with the Boussinesq approximation [DR04], utilized to account for the buoyancy effects due to temperature variations. This approximation states that the fluid's density varies with temperature but remains virtually unaffected by pressure, as discussed above. The coefficient  $\beta$  [K<sup>-1</sup>] is the fluid volume expansion coefficient, and  $\vec{g}$  [m s<sup>-2</sup>] the gravitational acceleration vector. As the variation of temperature is small, we can consider that the density is constant in the fluid domain, and the Boussinesq approximation is valid. Depending on the position of the patient (standing, laying supine or prone respectively),  $\vec{g}$  can be either vertical ( $\vec{g} = [0, -g, 0]^T$ ) or horizontal ( $\vec{g} = [g, 0, 0]^T$ ,  $\vec{g} = [-g, 0, 0]^T$  respectively), where  $g$  is the gravitational acceleration.

We impose no-slip boundary conditions for the fluid velocity on the boundaries of  $\Omega_{\text{AH}}$ :

$$\vec{u} = \vec{0} \quad \text{on } \Gamma_C \cup \Gamma_I \cup \Gamma_L \cup \Gamma_{\text{VH}} \cup \Gamma_{\text{Sc}}. \quad (3)$$

These boundary conditions, together with Eq. (1), model the AH flow driven by thermal and gravitational effects. The hydraulic pressure difference due to the production and drainage of AH is not explicitly accounted for, as previous studies have indicated that buoyancy is the dominant mechanism driving convective motion in the AH regardless of postural orientation [ON08; Kum+06].

Note that alternative boundary conditions, such as non-homogeneous Dirichlet conditions [HB02; Abd+21] or specified flow rates and pressures [Wan+16], could also be considered but are beyond the scope of the present study.

Moreover, the heat transfer inside the eye is governed by the heat equation (1c), with the following boundary conditions, taking into account the convective heat transfer with the surrounding tissues over a domain denoted as  $\Gamma_{\text{body}}$ ; and the heat production due to the metabolism of the eye, as well as the heat transfer with the ambient air over a domain called  $\Gamma_{\text{amb}}$ :

$$-k \frac{\partial T}{\partial \vec{n}} = h_{\text{bl}}(T - T_{\text{bl}}) \quad \text{on } \Gamma_{\text{body}}, \quad (4a)$$

$$-k \frac{\partial T}{\partial \vec{n}} = \underbrace{h_{\text{amb}}(T - T_{\text{amb}})}_{(i)} + \underbrace{\sigma \varepsilon (T^4 - T_{\text{amb}}^4)}_{(ii)} + \underbrace{E}_{(iii)} \quad \text{on } \Gamma_{\text{amb}}, \quad (4b)$$

where  $\Gamma_{\text{body}}$  and  $\Gamma_{\text{amb}}$  are the boundaries of the eye in contact with the surrounding body and the ambient air, respectively.

Precisely, Eq. (4a) models the convective heat transfer between the eye and the surrounding body, where  $h_{\text{bl}}$  [ $\text{W m}^{-2} \text{K}^{-1}$ ] is the heat transfer coefficient between the eye and the surrounding body, and  $T_{\text{bl}}$  [K] is the blood temperature. On the other hand, Eq. (4b) models three types of exchanges that are involved between the eyeball and the ambient air: (i) Convective heat transfer, where  $h_{\text{amb}}$  [ $\text{W m}^{-2} \text{K}^{-1}$ ] is the heat transfer coefficient between the eye and the ambient air, and  $T_{\text{amb}}$  [K] is the ambient temperature; (ii) radiative heat transfer, where  $\sigma = 5.67 \times 10^{-8} \text{ W/m}^2/\text{K}^4$  represents the Stefan-Boltzmann constant, and  $\varepsilon$  [-] is the emissivity of the cornea; and (iii) evaporative heat loss, due to tear evaporation at the surface of the eye, where  $E$  [ $\text{W m}^{-2}$ ] is the evaporation rate of the tear film.

**Remark 1.** *The momentum Eq. (1a) could be further simplified by discarding the contribution of the non-linear term  $\rho(\vec{u} \cdot \nabla)\vec{u}$ , and considering a Stokes flow, since the Reynolds number is reported to be relatively small in this case, see for instance [Wan+16]. However, due to the coupling with the heat equation in the system, an iterative approach is still required to solve the problem. Moreover, several other works [Abd+21; Wan+16] consider the full Navier-Stokes equations, and therefore we utilized the same model for consistency and comparison. We performed a comparative study of different modeling approaches, that is presented among results in Section 4.*

### 3 Mathematical and computational framework

In this section, we present the mathematical and computational framework developed to solve the coupled fluid dynamics and heat transfer model described in Eqs. (1), (3) and (4). We detail the variational formulation in Section 3.1, the geometrical and finite element discretization in Sections 3.2 and 3.3 respectively, and the solution strategy employed in Section 3.4.

#### 3.1 Continuous setting

We begin by deriving the variational formulation of the model. Let us introduce the following functional spaces:

- (i) The velocity space  $\mathbf{V} := [H_0^1(\Omega_{\text{AH}})]^3$ , consisting of vector fields  $\vec{u}$  with square-integrable derivatives with a trace that vanishes on the boundary;
- (ii) the pressure space  $Q := L_0^2(\Omega_{\text{AH}}) = \left\{ p \in L^2(\Omega_{\text{AH}}) \mid \int_{\Omega_{\text{AH}}} p \, d\vec{x} = 0 \right\}$ , consisting of square-integrable scalar fields with zero mean; and
- (iii) the temperature space  $W := H^1(\Omega)$ .

Let  $\vec{v} \in \mathbf{V}$ ,  $q \in Q$ , and  $\varphi \in W$  be test functions. Multiplying Equations (1a), (1b), and (1c) by  $\vec{v}$ ,  $q$ , and  $\varphi$ , respectively, and integrating by part over the appropriate domains yield:

$$\begin{aligned} \rho \int_{\Omega_{\text{AH}}} (\vec{u} \cdot \nabla) \vec{u} \cdot \vec{v} \, d\vec{x} + \mu \int_{\Omega_{\text{AH}}} \underline{\underline{D}}(\vec{u}) : \nabla \vec{v} \, d\vec{x} - \int_{\Omega_{\text{AH}}} p \cdot \nabla \vec{v} \, d\vec{x} \\ + \int_{\Omega_{\text{AH}}} \rho_0 \beta T \vec{g} \cdot \vec{v} \, d\vec{x} = \int_{\Omega_{\text{AH}}} \rho_0 \beta T_{\text{ref}} \vec{g} \cdot \vec{v} \, d\vec{x}, \end{aligned} \quad (5a)$$

$$\int_{\Omega_{\text{AH}}} \nabla \cdot \vec{u} q \, d\vec{x} = 0, \quad (5b)$$

$$\begin{aligned} \rho C_p \int_{\Omega} \vec{u} \cdot \nabla T \varphi \, d\vec{x} + k \int_{\Omega} \nabla T \cdot \nabla \varphi \, d\vec{x} + \int_{\Gamma_{\text{amb}}} (h_{\text{amb}} T \, d\sigma + \sigma \varepsilon T^4) \varphi \, d\sigma + \int_{\Gamma_{\text{body}}} h_{\text{bl}} T \varphi \, d\sigma \\ = \int_{\Gamma_{\text{amb}}} (h_{\text{amb}} T_{\text{amb}} + \sigma \varepsilon T_{\text{amb}}^4) \varphi \, d\sigma + \int_{\Gamma_{\text{body}}} h_{\text{bl}} T_{\text{bl}} \varphi \, d\sigma. \end{aligned} \quad (5c)$$

We define the following bilinear and trilinear forms:

$$a_1(\vec{z}, \vec{u}, \vec{v}) = \rho \int_{\Omega_{\text{AH}}} (\vec{z} \cdot \nabla) \vec{u} \cdot \vec{v} \, d\vec{x}, \quad (6a)$$

$$a_2(\vec{u}, \vec{v}) = \mu \int_{\Omega_{\text{AH}}} \underline{\underline{D}}(u) : \nabla \vec{v} \, d\vec{x}, \quad (6b)$$

$$b(p, \vec{v}) = - \int_{\Omega_{\text{AH}}} p \cdot \nabla \vec{v} \, d\vec{x}, \quad (6c)$$

$$d(T, \vec{v}) = - \int_{\Omega_{\text{AH}}} \rho_0 \beta T \vec{g} \cdot \vec{v} \, d\vec{x}, \quad (6d)$$

$$e(\vec{u}, T, \phi) = \rho C_p \int_{\Omega} \vec{u} \cdot \nabla T \phi \, d\vec{x}, \quad (6e)$$

$$f(T, \phi) = k \int_{\Omega} \nabla T \cdot \nabla \phi \, d\vec{x} + \int_{\Gamma_{\text{amb}}} (h_{\text{amb}} T + \sigma \varepsilon T^4) \phi \, d\sigma + \int_{\Gamma_{\text{body}}} h_{\text{bl}} T \phi \, d\sigma, \quad (6f)$$

$$\ell_1(\vec{v}) = \int_{\Omega_{\text{AH}}} \rho_0 \beta T_{\text{ref}} \vec{g} \cdot \vec{v} \, d\vec{x}, \quad (6g)$$

$$\ell_2(\phi) = \int_{\Gamma_{\text{amb}}} (h_{\text{amb}} T_{\text{amb}} + \sigma \varepsilon T_{\text{amb}}^4) \phi \, d\sigma + \int_{\Gamma_{\text{body}}} h_{\text{bl}} T_{\text{bl}} \phi \, d\sigma. \quad (6h)$$

The variational formulation of the problem is then: Find  $(\vec{u}, p, T) \in \mathbf{V} \times Q \times W$  such that for all  $(\vec{v}, q, \varphi) \in \mathbf{V} \times Q \times W$ :

$$\begin{aligned} a_1(\vec{u}, \vec{u}, \vec{v}) + a_2(\vec{u}, \vec{v}) + b(p, \vec{v}) + d(T, \vec{v}) &= \ell_1(\vec{v}), \\ b(q, \vec{u}) &= 0, \\ e(\vec{u}, T, \phi) + f(T, \phi) &= \ell_2(\phi). \end{aligned} \quad (7)$$

**Theorem 1** (Existence and Uniqueness). *The variational problem (7) has a unique solution.*

*Proof.* A detailed proof is beyond the scope of this work. However, the existence and uniqueness can be established using fixed-point arguments and standard results for the Navier-Stokes equations coupled with heat transfer, as discussed in [Tsu15].  $\square$

### 3.2 Geometrical discretization

The geometry presented in Fig. 1(a) is discretized, with significant effort devoted to the AC and PC domains, where the coupled fluid-thermal problem is solved. This meticulous approach ensures that the complexities of these regions are accurately captured, leading to more precise simulation results. The discretization results in a mesh composed of  $4.97 \cdot 10^6$  elements, highlighting the level of detail and refinement applied to the model. The mesh refinement is presented among results in Fig. 6. Such detailed refinement is essential for resolving the interactions between fluid flow and thermal dynamics within these areas, thereby improving the overall accuracy and reliability of the simulation outcomes. A few remarks are in order in practice: (i) the mesh generation is done *via* [CAS22], (ii) the mesh adaptations and refinements are performed using [MMG22] and the level set features of Feel++ [Pru+24], (iii) the mesh is not only refined to obtain a hierarchy of increasingly refined meshes but also adapted along the boundaries to obtain a graded mesh with respect to the distance to the boundaries, thanks to the level set features above-mentioned. The latter feature is particularly important to obtain accurate surface quantities' approximation, such as the wall shear stress.

A complete description of the mesh generation and adaptation process is available in [Cha+24]. Moreover, the family of meshes is available publicly [Sai+24b].

### 3.3 Finite element setting

We discretize the variational problem using the finite element method (FEM). The computational domain is discretized as described in [Cha+24], with mesh refinement in the anterior and posterior chambers to accurately capture the flow and thermal dynamics.

We define the finite element spaces for velocity, pressure, and temperature as follows:

- $\mathbf{V}_h := \{\vec{v} \in [\mathbb{P}_2(\Omega_{\text{AH}})]^3 \mid \vec{v} = \vec{0} \text{ on } \partial\Omega\}$ , the space of vector-valued piecewise quadratic polynomials that vanish on the boundary for velocity;
- $Q_h := \mathbb{P}_1(\Omega_{\text{AH}})$ , the space of piecewise linear polynomials for pressure; and
- $W_h := \mathbb{P}_1(\Omega)$ , the space of piecewise linear polynomials for temperature.

This choice corresponds to the  $\mathbb{P}_1$ - $\mathbb{P}_2$ - $\mathbb{P}_1$  Taylor-Hood element for the velocity-pressure pair, which satisfies the LBB (Ladyzhenskaya-Babuška-Brezzi) stability condition [ESW14]. Other discretization strategies could be employed, such as  $\mathbb{P}_1$ - $\mathbb{P}_1$  or  $\mathbb{P}_2$ - $\mathbb{P}_2$ - $\mathbb{P}_1$ . The former requires a stabilization term to ensure stability, while the latter is more computationally expensive and may not provide significant improvements in accuracy.

The discrete problem reads: Find  $(\vec{u}_h, p_h, T_h) \in \mathbf{V}_h \times Q_h \times W_h$  such that for all  $(\vec{v}_h, q_h, \varphi_h) \in \mathbf{V}_h \times Q_h \times W_h$ :

$$\begin{cases} a_1(\vec{u}_h, \vec{u}_h, \vec{v}_h) + a_2(\vec{u}_h, \vec{v}_h) + b(p_h, \vec{v}_h) + d(T_h, \vec{v}_h) = \ell_1(\vec{v}_h), \\ b(q_h, \vec{u}_h) = 0, \\ e(\vec{u}_h, T_h, \varphi_h) + f(T_h, \varphi_h) = \ell_2(\varphi_h). \end{cases} \quad (8)$$

The system (8) is non-linear because of the terms  $a_1$  and  $e$ . We employ Newton's method to solve it iteratively. Precisely, it consists of starting from an initial guess  $(\vec{u}^0, p^0, T^0)$ , and iteratively compute  $(\vec{u}^{k+1}, p^{k+1}, T^{k+1})$  as the solution of the non-linear system at each iteration. We set the correction terms  $\delta\vec{u}^k := \vec{u}^{k+1} - \vec{u}^k$ ,  $\delta p^k := p^{k+1} - p^k$ , and  $\delta T^k := T^{k+1} - T^k$ . Given  $(\vec{u}^k, p^k, T^k)$ , we define the *nonlinear residual* associated with the variational formulation (8) as:

$$\begin{cases} r_{\vec{u}}^k(\vec{v}) := \ell_1(\vec{v}) - a_1(\vec{u}^k, \vec{u}^k, \vec{v}) - a_2(\vec{u}^k, \vec{v}) - b(p^k, \vec{v}) - d(T^k, \vec{v}), \\ r_p^k(q) := -b(q, \vec{u}^k), \\ r_T^k(\varphi) := \ell_2(\varphi) - e(\vec{u}^k, T^k, \varphi) - f(T^k, \varphi). \end{cases} \quad (9)$$

Following [ESW14, Ch. 8], by dropping the quadratics terms, the correction terms verify the following weak linear problem:  $\forall(\vec{v}, q, \varphi) \in \mathbf{V} \times Q \times T$ :

$$\begin{cases} a_1(\delta\vec{u}^k, \vec{u}^k, \vec{v}) + a_1(\vec{u}^k, \delta\vec{u}^k, \vec{v}) + a_2(\delta\vec{u}^k, \vec{v}) + b(\delta p^k, \vec{v}) + d(\delta T^k, \vec{v}) = r_{\vec{u}}^k(\vec{v}), \\ b(\delta p^k, \vec{u}^k) = r_p^k(q), \\ e(\delta\vec{u}^k, T^k, \varphi) + e(\vec{u}^k, \delta T^k, \varphi) + f(\delta T^k, \varphi) = r_T^k(\varphi). \end{cases} \quad (10)$$

In the discretized spaces  $\mathbf{V}_h \times Q_h \times T_h$ , the discrete counterpart of this variational problem is solved. To define the corresponding linear algebra problem, we set the basis of the discrete spaces:  $\{\vec{\lambda}_i\}_{i=1}^{N_u}$  is a basis of  $\mathbf{V}_h$ ,  $\{\mu_j\}_{j=1}^{N_p}$  is a basis of  $Q_h$ , and  $\{\xi_l\}_{l=1}^{N_T}$  is a basis of  $T_h$ . Setting  $\mathbf{u}$ ,  $\Delta\mathbf{u}$ ,  $\mathbf{p}$ ,  $\Delta\mathbf{p}$ ,  $\mathbf{T}$ , and  $\Delta\mathbf{T}$  the vectors of the coefficients of the basis functions in the corresponding basis of  $\vec{u}$ ,  $\delta\vec{u}$ ,  $p$ ,  $\delta p$ ,  $T$ , and  $\delta T$  respectively, the algebraic problem reads:

$$\begin{bmatrix} \underline{\mathbf{V}}^k + \underline{\mathbf{W}}^k + \underline{\mathbf{N}} & \underline{\mathbf{B}}^T & \underline{\mathbf{D}} \\ \underline{\mathbf{B}} & \underline{\mathbf{0}} & \underline{\mathbf{0}} \\ \underline{\mathbf{E}}_1^k & \underline{\mathbf{0}} & \underline{\mathbf{E}}_2^k + \underline{\mathbf{F}} \end{bmatrix} \begin{bmatrix} \Delta\mathbf{u} \\ \Delta\mathbf{p} \\ \Delta\mathbf{T} \end{bmatrix} = \begin{bmatrix} \mathbf{r}_{\vec{u}}^k \\ \mathbf{r}_p^k \\ \mathbf{r}_T^k \end{bmatrix}, \quad (11)$$

where all elements of this system are defined on the basis of the discrete spaces:

$$\begin{aligned} \underline{\mathbf{V}}^k &= [a_1(\vec{u}^k, \vec{\lambda}_i, \vec{\lambda}_j)] \in \mathbb{R}^{N_u \times N_u}, & \underline{\mathbf{W}}^k &= [a_1(\vec{\lambda}_i, \vec{u}^k, \vec{\lambda}_j)] \in \mathbb{R}^{N_u \times N_u}, & \underline{\mathbf{N}} &= [a_2(\vec{\lambda}_i, \vec{\lambda}_j)] \in \mathbb{R}^{N_u \times N_u}, \\ \underline{\mathbf{B}} &= [b(\mu_i, \vec{\lambda}_j)] \in \mathbb{R}^{N_p \times N_u}, & \underline{\mathbf{D}} &= [d(\vec{\lambda}_i, \xi_l)] \in \mathbb{R}^{N_u \times N_T}, \\ \underline{\mathbf{E}}_1^k &= [e(\vec{\lambda}_i, T^k, \xi_l)] \in \mathbb{R}^{N_u \times N_T}, & \underline{\mathbf{E}}_2^k &= [e(\vec{u}^k, \xi_l, \xi_m)] \in \mathbb{R}^{N_T \times N_T}, & \underline{\mathbf{F}} &= [f(\xi_l, \xi_m)] \in \mathbb{R}^{N_T \times N_T}, \\ \mathbf{r}_{\vec{u}}^k &= [r_{\vec{u}}^k(\vec{\lambda}_i)] \in \mathbb{R}^{N_u}, & \mathbf{r}_p^k &= [r_p^k(\mu_j)] \in \mathbb{R}^{N_p}, & \mathbf{r}_T^k &= [r_T^k(\xi_l)] \in \mathbb{R}^{N_T}. \end{aligned} \quad (12)$$

From the initial guess, we iteratively solve the linear algebra problem (11) at each Newton iteration, until the relative increment  $\text{Crit}^k := \max\{\|\delta\vec{u}^k\|/\|\delta\vec{u}^0\|, \|\delta p^k\|/\|\delta p^0\|, \|\delta T^k\|/\|\delta T^0\|\} \leq \varepsilon_{\text{tol}}$  is reached for a given tolerance  $\varepsilon_{\text{tol}} > 0$ . Algorithm 1 summarizes the Newton iteration loop.

The parameter  $\alpha \in [0, 1]$  is a relaxation factor that can be adjusted, using the line search method of PETSc [Bal+24], to improve the convergence of the Newton iteration.

---

**Algorithm 1:** Newton iteration loop.

---

**Input:**  $\{\mathbf{u}^0, \mathbf{p}^0, \mathbf{T}^0, \varepsilon_{\text{tol}}\}$ .  
 $(\mathbf{u}^0, \mathbf{p}^0, \mathbf{T}^0) \leftarrow$  initial guess;  
Assemble  $\underline{\underline{N}}, \underline{\underline{B}}, \underline{\underline{D}}, \underline{\underline{F}}$ ;  
**while**  $\text{Crit}^k > \varepsilon_{\text{tol}}$  **do**  
    Assemble  $\underline{\underline{V}}^k, \underline{\underline{W}}^k, \underline{\underline{E}}_1^k, \underline{\underline{E}}_2^k, \mathbf{r}_{\bar{u}}^k, \mathbf{r}_p^k, \mathbf{r}_T^k$ ;  
     $(\Delta \mathbf{u}, \Delta \mathbf{p}, \Delta \mathbf{T}) \leftarrow$  solution to System (11);  
     $\mathbf{u}^{k+1} \leftarrow \mathbf{u}^k + \alpha \Delta \mathbf{u}, \mathbf{p}^{k+1} \leftarrow \mathbf{p}^k + \alpha \Delta \mathbf{p}, \mathbf{T}^{k+1} \leftarrow \mathbf{T}^k + \alpha \Delta \mathbf{T}$ ;  
**end**  
**Output:**  $(\mathbf{u}^{k+1}, \mathbf{p}^{k+1}, \mathbf{T}^{k+1})$ .

---

### 3.4 Solution strategy

We implement the computational framework using the heatfluid toolbox of Feel++<sup>1</sup> [Pru+24] to solve Algorithm 1. Efficiently solving the resulting linear systems at each Newton iteration is crucial.

Direct solvers become impractical for large-scale problems due to computational and memory constraints. Therefore, we employ iterative solvers with appropriate preconditioners to enhance convergence. The preconditioner is a key component in the iterative solver, as it actually enables the solver to converge. We utilize a *field-split* preconditioning strategy, where the global system is partitioned into smaller blocks corresponding to different physical fields, namely fluid and thermal fields. This approach allows us to apply specialized solvers and preconditioners to each block.

For clarity, we rewrite the system (11) with block notation, omitting the superscript  $k$ :

$$\left[ \begin{array}{cc|c} \underline{\underline{\tilde{A}}} & \underline{\underline{B}}^T & \underline{\underline{D}} \\ \underline{\underline{B}} & \underline{\underline{0}} & \underline{\underline{0}} \\ \underline{\underline{E}} & \underline{\underline{0}} & \underline{\underline{F}} \end{array} \right] \left[ \begin{array}{c} \Delta \mathbf{u} \\ \Delta \mathbf{p} \\ \Delta \mathbf{T} \end{array} \right] = \left[ \begin{array}{c} \mathbf{r}_{\bar{u}} \\ \mathbf{r}_p \\ \mathbf{r}_T \end{array} \right] \iff \underbrace{\left[ \begin{array}{cc} \underline{\underline{K}}_{0,0} & \underline{\underline{K}}_{0,1} \\ \underline{\underline{K}}_{1,0} & \underline{\underline{K}}_{1,1} \end{array} \right]}_{=: \underline{\underline{K}}} \left[ \begin{array}{c} \Delta_{\text{fluid}} \\ \Delta_{\text{heat}} \end{array} \right] = \left[ \begin{array}{c} \mathbf{r}_{\text{fluid}} \\ \mathbf{r}_{\text{heat}} \end{array} \right]. \quad (13)$$

The main idea of *additive fieldsplit* preconditioner is to approximate the inverse of the matrix  $\underline{\underline{K}}$  by the matrix

$$\left[ \begin{array}{cc} \underline{\underline{K}}_{0,0}^{-1} & \underline{\underline{0}} \\ \underline{\underline{0}} & \underline{\underline{K}}_{1,1}^{-1} \end{array} \right], \quad (14)$$

where the inverses of the diagonal blocks are applied separately, with appropriate solvers and associated preconditioners.

The heat block  $\underline{\underline{K}}_{1,1}$  inverse is approximated using a few iterations of *GAMG* — Geometric Algebraic Multigrid — from PETSc [Bal+24]. This preconditioner efficiently handles large sparse matrices by recursively coarsening and solving the problem on multiple levels, significantly accelerating the convergence.

On the other hand, concerning the fluid block  $\underline{\underline{K}}_{0,0}$ , the inverse is approximated using the Schur complement, as proposed in [ESW14, Ch. 9], where another field split preconditioner is implemented: the degrees of freedom are now divided into velocity and pressure blocks. Then, the LDU decomposition of the matrix  $\underline{\underline{K}}_{0,0}$  is computed as follows:

$$\underline{\underline{K}}_{0,0} = \left[ \begin{array}{c|c} \underline{\underline{\tilde{A}}} & \underline{\underline{B}}^T \\ \underline{\underline{B}} & \underline{\underline{0}} \end{array} \right] = \underbrace{\left[ \begin{array}{cc} \underline{\underline{I}} & \underline{\underline{0}} \\ \underline{\underline{B}} \underline{\underline{A}}^{-1} & \underline{\underline{I}} \end{array} \right]}_{\underline{\underline{L}}} \underbrace{\left[ \begin{array}{cc} \underline{\underline{\tilde{A}}} & \underline{\underline{0}} \\ \underline{\underline{0}} & \underline{\underline{S}} \end{array} \right]}_{\underline{\underline{D}}} \underbrace{\left[ \begin{array}{cc} \underline{\underline{I}} & \underline{\underline{\tilde{A}}}^{-1} \underline{\underline{B}}^T \\ \underline{\underline{0}} & \underline{\underline{I}} \end{array} \right]}_{\underline{\underline{U}}}, \quad (15)$$

where  $\underline{\underline{S}} = -\underline{\underline{B}} \underline{\underline{\tilde{A}}}^{-1} \underline{\underline{B}}^T$  is the *Schur complement operator*. We employ here an *upper* strategy, namely we approximate the inverse of  $\underline{\underline{K}}_{0,0}$  by the matrix  $(\underline{\underline{D}} \underline{\underline{U}})^{-1}$ :

$$\underline{\underline{K}}_{0,0}^{-1} \approx \left[ \begin{array}{cc} \underline{\underline{I}} & -\underline{\underline{\tilde{A}}}^{-1} \underline{\underline{B}}^T \\ \underline{\underline{0}} & \underline{\underline{I}} \end{array} \right] \left[ \begin{array}{cc} \underline{\underline{\tilde{A}}}^{-1} & \underline{\underline{0}} \\ \underline{\underline{0}} & \underline{\underline{S}}^{-1} \end{array} \right]. \quad (16)$$

Note that these two matrices are not computed explicitly, as we are computing the action of the inverse on a vector. Finally, another fieldsplit is applied to the velocity block  $\underline{\underline{A}}$ , where the velocity components are solved separately using a block Jacobi preconditioner, decoupling the velocity components.

We summarize in Table 1 the preconditioners used for the different blocks of the system (11), as well as the Krylov Subspace Method (KSP) employed to solve the linear system. These methods can be either the *Generalized Minimal Residual* (GMRES) or the *Flexible GMRES* (FGMRES) methods, depending on the block being solved. In some cases,

<sup>1</sup>See documentation: <https://docs.feelpp.org/toolboxes/latest/heatfluid/>

Block	Description	Preconditioner	Krylov solver
$\underline{\underline{K}}$	Overall coupled problem	fieldsplit additive	gmres
$\underline{\underline{K}}_{-1,1}$	Heat split subproblem	gamg	gmres
$\underline{\underline{K}}_{0,0}$	Fluid split subproblem	fieldsplit schur	fgmres
$\underline{\underline{A}}$	Velocity block (split)	jacobi	preonly
$\underline{\underline{S}}$	Schur complement	gamg	preonly

Table 1: Description of the solvers and preconditioners used for the different blocks of the system (11). In monospaced font, we indicate the actual PETSc component used for the solver and preconditioner used.

Parameter	Value	Dimension	Parameter	Value	Dimension
$\mu$	0.001	$[\text{kg m}^{-1} \text{s}^{-1}]$	$T_{\text{bl}}$	310	$[\text{K}]$
$\rho$	1000	$[\text{kg m}^{-3}]$	$T_{\text{amb}}$	294	$[\text{K}]$
$C_p$	4178	$[\text{J kg}^{-1} \text{K}^{-1}]$	$k_{\text{lens}}$	0.4	$[\text{W m}^{-1} \text{K}^{-1}]$
$\beta$	$3 \cdot 10^{-4}$	$[\text{K}^{-1}]$	$k_{\text{cornea}}$	0.58	$[\text{W m}^{-1} \text{K}^{-1}]$
$g$	9.81	$[\text{m s}^{-2}]$	$k_{\text{sclera}} = k_{\text{iris}} =$ $k_{\text{lamina}} = k_{\text{opticNerve}}$	1.0042	$[\text{W m}^{-1} \text{K}^{-1}]$
$T_{\text{ref}}$	298	$[\text{K}]$	$k_{\text{aqueousHumor}}$	0.28	$[\text{W m}^{-1} \text{K}^{-1}]$
$h_{\text{bl}}$	65	$[\text{W m}^{-2} \text{K}^{-1}]$	$k_{\text{vitreousHumor}}$	0.603	$[\text{W m}^{-1} \text{K}^{-1}]$
$h_{\text{amb}}$	10	$[\text{W m}^{-2} \text{K}^{-1}]$	$k_{\text{choroid}} = k_{\text{retina}}$	0.52	$[\text{W m}^{-1} \text{K}^{-1}]$
$E$	40	$[\text{W m}^{-3}]$	$\varepsilon$	0.975	$[-]$

Table 2: Parameters used for the simulations, representing nominal physiological values. Sources can be found in [ON08; Wan+16; SPS24].

the `preonly` solver is used, which indicates that no Krylov subspace solver is executed, rather only the associated preconditioner is applied once. More details on the setting of these preconditioners can be found in the configuration file presented in [Sai+24b].

## 4 Verification and validation of the proposed model

In this section, we present the verification and validation of our proposed model through numerical simulations conducted using the computational framework detailed in Section 3. The simulations aim to verify the accuracy and reliability of our model in replicating the physiological conditions of the human eye. The set of parameters used in the simulations is listed in Table 2, representing nominal physiological values corresponding to a healthy subject.

All the results presented in this document are available and can be reproduced, refer to Section 6 for more details. All subsequent computational simulations are performed on the same machine, named *Gaya*, equipped with the following hardware: **6 nodes with 2 AMD EPYC 7713 64-Core Processors and 512 MB of RAM.**

To ensure the accuracy and reliability of our numerical solutions, we first perform a mesh convergence analysis, followed by a scalability study to assess the computational performance of our framework. We also compare our results with those from prior research to further validate our model.

**Remark 2.** *Regarding the choice of the model discussed in Remark 1, we perform a comparative study of different modeling approaches, comparing computational times for assembly and solution phases, as summarized in Table 3. While the use of linearized boundary conditions in the sense of [Sco88], where the radiative heat transfer condition is approximated by a linear Robin condition, and the Stokes equations slightly reduced the computational time, the differences were not substantial. Thus, we opted to use the fully non-linear Navier-Stokes equations to maintain the accuracy of the model.*

*The computational times indicate that while linear boundary conditions and the Stokes model reduce solution time, the fully non-linear Navier-Stokes model provides a more accurate representation of the AH dynamics with only a modest increase in computational effort.*

### 4.1 Mesh convergence analysis: ensuring accuracy and reliability

To verify the accuracy of our numerical solution, we conduct a mesh convergence study. We generate a series of meshes, denoted `Mr0` to `Mr5`, with progressively increasing levels of refinement, following the procedure described in [Cha+24]. The characteristics of these meshes, including the minimum, maximum, and mean element sizes, the number of elements, and the degrees of freedom for temperature, velocity, and pressure fields, are summarized in Table 4.



Table 3: Comparison of computational times for different models, using mesh **Mr4** parallelized on 256 cores.

(a) Time to assembly the algebraic objects.				(b) Time to solve the problem.		
Model	Boundary condition	Time [s]		Model	Boundary condition	Time [s]
Navier-Stokes	Non-linear	0.24		Navier-Stokes	Non-linear	68.89
Navier-Stokes	Linear	0.25		Navier-Stokes	Linear	43.7
Stokes	Non-linear	0.24		Stokes	Non-linear	69.14
Stokes	Linear	0.26		Stokes	Linear	46.2

M	$h_{\min}$	$h_{\max}$	$h_{\text{mean}}$	# elements	# Degree of freedom		
					$T$	$\vec{u}$	$p$
<b>Mr0</b>	$1.25 \cdot 10^{-4}$	$4 \cdot 10^{-3}$	$9.23 \cdot 10^{-4}$	$1.92 \cdot 10^5$	37,470	84,966	4,615
<b>Mr1</b>	$1.37 \cdot 10^{-4}$	$3.63 \cdot 10^{-3}$	$7.72 \cdot 10^{-4}$	$2.82 \cdot 10^5$	51,753	$1.17 \cdot 10^5$	6,155
<b>Mr2</b>	$6.54 \cdot 10^{-5}$	$1.6 \cdot 10^{-3}$	$4.67 \cdot 10^{-4}$	$7.47 \cdot 10^5$	$1.31 \cdot 10^5$	$5.9 \cdot 10^5$	28,548
<b>Mr3</b>	$3.29 \cdot 10^{-5}$	$9.59 \cdot 10^{-4}$	$4.17 \cdot 10^{-4}$	$1.4 \cdot 10^6$	$2.42 \cdot 10^5$	$7.08 \cdot 10^5$	34,304
<b>Mr4</b>	$2.55 \cdot 10^{-5}$	$5.29 \cdot 10^{-4}$	$2.88 \cdot 10^{-4}$	$6.04 \cdot 10^6$	$1.03 \cdot 10^6$	$1.02 \cdot 10^6$	48,534
<b>Mr5</b>	$3.12 \cdot 10^{-5}$	$1.5 \cdot 10^{-4}$	$2.77 \cdot 10^{-4}$	$4.39 \cdot 10^7$	$7.37 \cdot 10^6$	$4.62 \cdot 10^6$	$2.05 \cdot 10^5$
<b>Mr6</b>	$2.82 \cdot 10^{-5}$	$9.94 \cdot 10^{-7}$	$1.84 \cdot 10^{-4}$	$1.51 \cdot 10^8$	$2.52 \cdot 10^7$	$1.47 \cdot 10^7$	$6.37 \cdot 10^5$

Table 4: Characteristics of meshes used for the convergence study and number of degrees of freedom for temperature  $T$ , velocity  $\vec{u}$ , and pressure  $p$  respectively, using  $\mathbb{P}_1$ – $\mathbb{P}_2\mathbb{P}_1$  elements.

Using these meshes, we solve the model equations with consistent parameters and boundary conditions. We extract quantities of interest from the solutions, namely the maximum temperature of the cornea and the mean velocity of the aqueous humor in the anterior chamber. The evolution of these quantities with respect to the number of degrees of freedom is presented in Fig. 3.

As shown in Fig. 3, both the maximum corneal temperature and the mean aqueous humor velocity converge toward asymptotic values as the mesh is refined. This convergence indicates that our numerical solution becomes independent of the mesh size, confirming the accuracy and reliability of the simulation results. We observe that beyond a certain mesh density, further refinement results in negligible changes in the computed quantities, suggesting that an optimal mesh size can be selected to balance accuracy and computational cost.

Based on these results, we select mesh **Mr4** for subsequent simulations, using the  $\mathbb{P}_1$ – $\mathbb{P}_2\mathbb{P}_1$  discretization, as it provides a good compromise between accuracy and computational efficiency.

## 4.2 Speed-up and scalability study

We assess the scalability of our computational framework by measuring the execution time required to solve the model as a function of the number of MPI parallel processes utilized. This analysis provides insights into the efficiency and performance of our implementation on parallel computing architectures.

**Impact of the postural orientation** We first examine the scalability in the context of different postural orientations of the eye—standing, prone, and supine. The execution times required to assemble and solve the non-linear problem (as outlined in Algorithm 1) for each posture are presented in Fig. 4(a). As anticipated, the execution time decreases with an increasing number of parallel processes, demonstrating the benefits of parallelization.

Notably, the simulation for the standing position requires more time compared to the prone and supine positions. This difference is attributed to the higher fluid velocities observed in the standing position, which necessitate more non-linear iterations for convergence (five iterations compared to four for the other positions).

We compute the speed-up  $s = t_1/t_{\text{np}}$ , where  $t_1$  is the execution time with a single process, and  $t_{\text{np}}$  is the time with  $\text{np}$  parallel processes. The results, depicted in Fig. 4(b), show that while the speed-up improves with additional processes, it deviates from the ideal linear speed-up, particularly at higher process counts. The performance degradation is due to the increased communication overhead and synchronization costs associated with parallelization, which become more pronounced as the number of processes grows.

Overall, our computational framework demonstrates effective scalability across different simulation scenarios, with parallelization yielding significant reductions in execution time.

**Scalability analysis of simulation components** Beyond the assembly and solution phases, we investigate the scalability of other key components of the simulation. Focusing on the three largest meshes (**Mr4**, **Mr5**, and **Mr6**), we measure the execution times for the following steps:

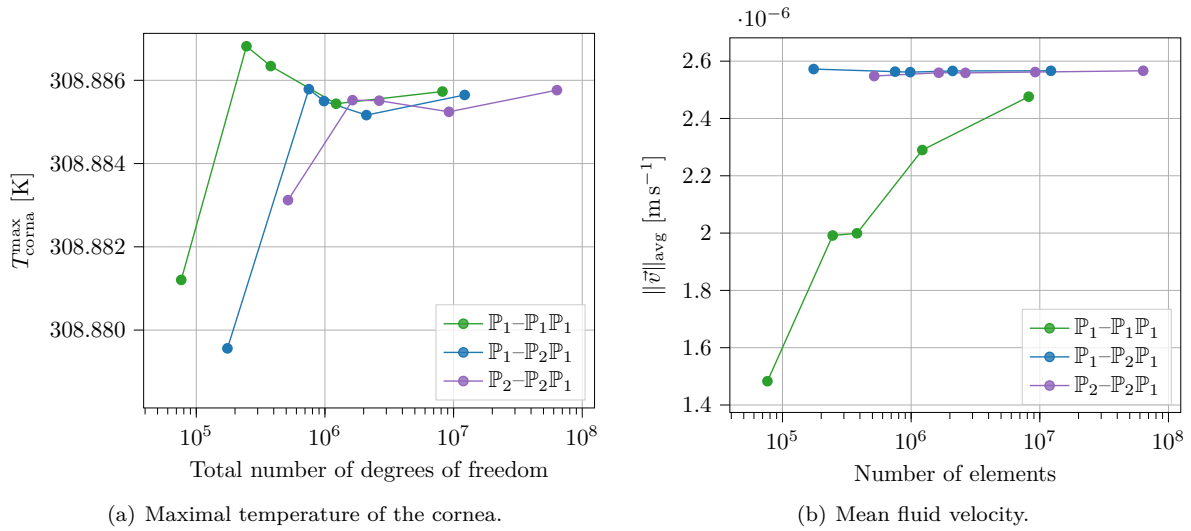


Figure 3: Results of the mesh convergence study. For each curve, the point on the left corresponds to mesh **Mr1**, and the point on the right to mesh **Mr5**. The reference quantity used to compute the relative error as been obtained with the mesh **Mr5** and the discretization  $\mathbb{P}_2\text{-}\mathbb{P}_2\mathbb{P}_1$ , and a higher order of accuracy required to the solver.

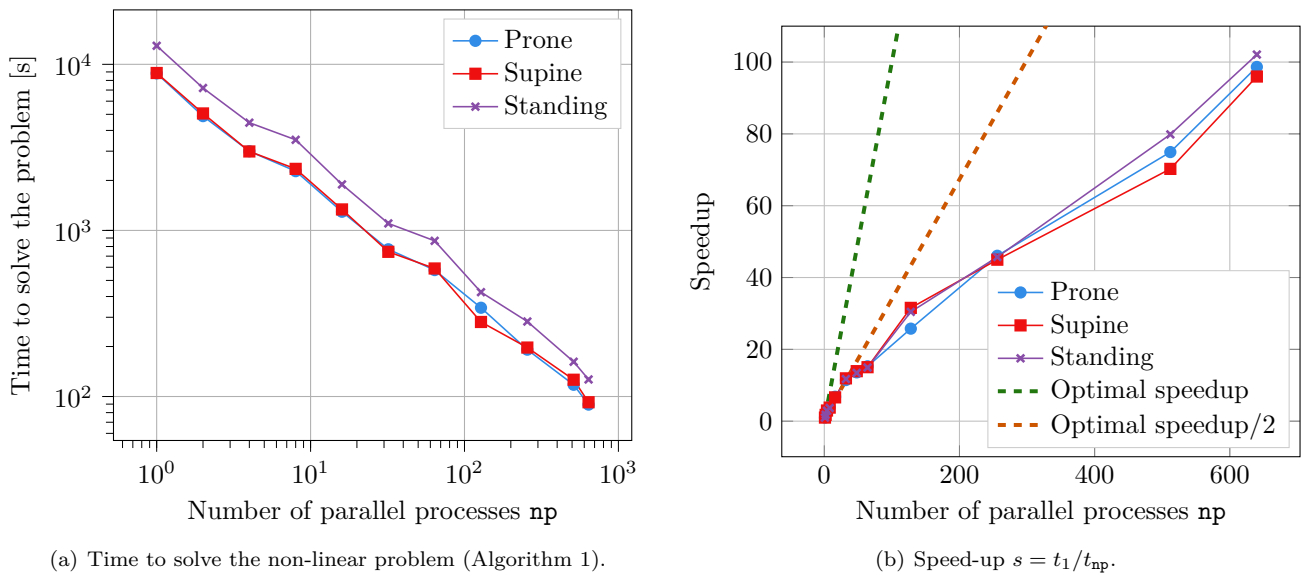
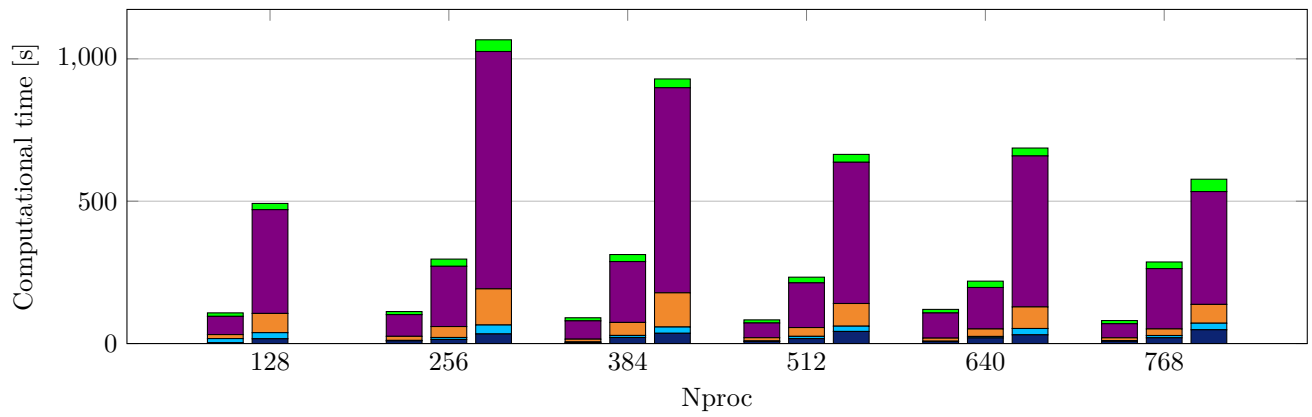
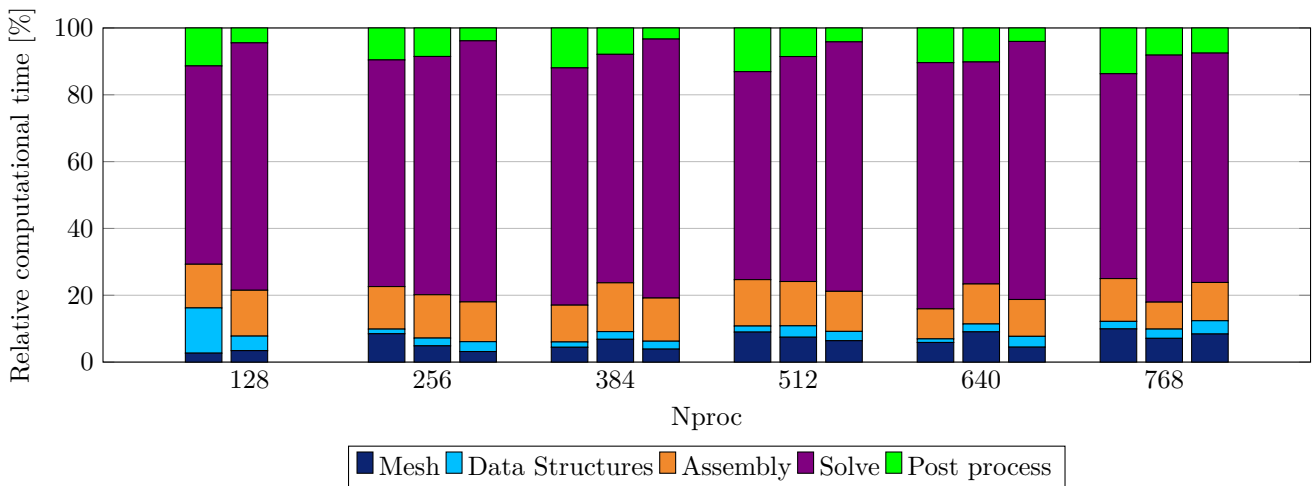


Figure 4: Scalability results: time of execution to simulate coupled model (left panel), and corresponding speed-up, for an increasing number of parallel processes, and for the three subject positions (right panel).



(a) Absolute computational time in each component.



(b) Relative time in each component.

Figure 5: Absolute and relative computational time for the coupled heat-fluid test case in the standing position, performed on Gaya with the meshes **Mr4** (left), **Mr5** (middle), and **Mr6** (right).

- (i) Load and initialize the mesh that is already partitioned on the disk: this step involves reading the pre-partitioned mesh data from the disk and initializing the mesh structure in memory.
- (ii) Initialize the data structures: this step sets up the necessary data structures required for the simulation, including matrices, vectors, and other computational entities.
- (iii) Assemble the algebraic objects of the linear system: this step involves assembling the linear system of equations that arise from the discretization of the governing equations.
- (iv) Solve the non-linear algebraic system: this step involves solving the non-linear equations that arise from the discretization of the governing equations using iterative solvers.
- (v) Export the results: this step writes the computed results, such as temperature, velocity, and pressure fields, to disk in the specified output format.

The execution times and their relative contributions are summarized in Fig. 5. We selected for this analysis the standing position, which is the most challenging case. The resolution of the non-linear system is the most time-consuming step, followed by the assembly phase. As the number of processes increases, we observe a decrease in execution times for most components, except for the result export phase, where I/O operations become a bottleneck due to the larger data volumes and potential disk access contention.

These findings highlight the importance of optimizing not only the computational algorithms but also the data management strategies, particularly for large-scale simulations.

### 4.3 Validation in comparison with previous studies

To validate our model, we compare our results with those from previous studies that have investigated temperature distributions and AH flow in the human eye. Notably, [Sco88] developed a 2D heat transfer model, [ON08] extended

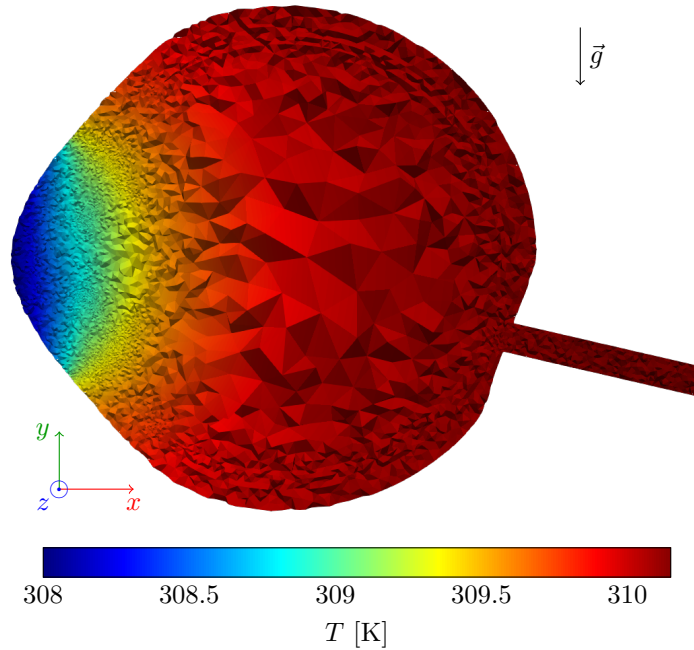


Figure 6: Distribution of the computed temperature over the eyeball in the standing position, on a vertical cut. Mesh discretization is also presented.

Reference	$T_{\text{amb}}$	No AH flow	With consideration of the AH flow		
			Prone	Supine	Standing
Scott [Sco88] (2D)	293.15	306.4	n/a	n/a	n/a
Ooi and Ng [ON08] (2D)	298	306.45	n/a	n/a	306.9
Karampatzakis and Samaras [KS10] (3D)	293	306.81	n/a	n/a	307.06
	296	307.33	n/a	n/a	307.51
	298	307.69	n/a	n/a	307.83
Current model (3D)	293	306.5647	306.56915	306.55899	306.63672
	296	307.09845	307.10175	307.09436	307.14651
	298	307.45746	307.46008	307.45432	307.49222

Table 5: Corneal surface temperature (in K) for various configurations, comparison with numerical results from literature. A red value represents the highest temperature, and a blue value the lowest.

this to a 2D model coupling heat transfer with AH flow, and [KS10; Wan+16] presented a 3D coupled model, providing corneal temperatures for various ambient temperatures ( $T_{\text{amb}}$ ). Note that the first two studies only consider the standing position of the subject.

We focus first on the temperature results. Fig. 6 illustrates the computed temperature distribution over the eyeball in the standing position, depicted on a vertical cross-sectional plane. As expected, the temperature is higher in the posterior part of the eye, which is insulated within the body, and lower in the anterior region, where heat exchange with the ambient air occurs through the cornea. This temperature gradient aligns with observations reported in previous studies [ON08; Wan+16], reinforcing the validity of our model.

Table 5 presents the corneal surface temperatures from these studies alongside our findings for the three postural configurations. Consistently with previous research, we observe that coupling the AH flow leads to an increase in the corneal surface temperature in the standing position. While [KS10] reported a temperature difference of approximately 0.2K due to the flow, our model predicts a smaller difference of about 0.05 K. This discrepancy may be attributed to differences in model assumptions, boundary conditions, or computational methods.

Moreover, our results indicate that the lying positions (prone and supine) have minimal impact on the corneal temperature, with differences less than 0.01 K. Interestingly, we observe a slight decrease in corneal temperature in the prone position compared to the supine position, which can be explained by the flow patterns influenced by gravity, see Section 4.

Additionally, experimental studies compiled by [EYB89] and [NO06] report an average corneal surface temperature

Position	Reference	Maximum velocity [m s <sup>-1</sup> ]	Average velocity [m s <sup>-1</sup> ]	Pressure [mmHg]
Supine	[Wan+16]	$9.44 \cdot 10^{-4}$	$4.1 \cdot 10^{-5}$	13.50 – 13.58
	[Mur+23]	$6 \cdot 10^{-5}$	n/a	n/a
	[BBS20]	n/a	$9.88 \cdot 10^{-6}$	n/a
	Current model	$2.59 \cdot 10^{-5}$	$3.21 \cdot 10^{-6}$	15.42 – 15.59
Standing	[Wan+16]	$9.6 \cdot 10^{-4}$	$2.5 \cdot 10^{-4}$	13.50 – 13.59
	[BBS20]	n/a	$5.88 \cdot 10^{-5}$	n/a
	Current model	$2.76 \cdot 10^{-4}$	$5.23 \cdot 10^{-5}$	15.28 – 15.72

Table 6: Fluid velocity and pressure for various configurations, comparison with numerical results from literature.

of approximately 307.15 K, which falls within the range of our simulation results, further supporting the validity of our model. Note that the value of  $T_{\text{amb}}$  was not specified in the publications, but still, our findings lie within the interval of results reported.

Next, we analyze our findings on the AH flow. We present in Fig. 7 the velocity field and pressure distribution in the AC and PC for the three postural orientations. Note that as the pressure is defined up to a constant, we adjust it to a nominal value of 15.5 mmHg for comparison purposes, as this is a typical value for the intraocular pressure in healthy eyes. We present in Table 6 a comparison of the results with previous studies. We observe similar orders of magnitude and trends in the pressure and velocity distributions, which further validate our model, although differences in the exact values might persist, due to inherent differences in the modeling and computational process.

As a further assessment of the accuracy of the coupling between the fluid dynamics flow and the heat transfer model, we analyze the impact of a temperature difference on the fluid flow. Specifically, in [Can+02], the authors used a simple analytical model based on lubrication theory, and show the  $u_{\text{max}} \approx \Delta T \cdot 1.98 \cdot 10^{-4} \text{ m s}^{-1} \text{ K}^{-1}$ , where  $\Delta T$  is the temperature difference between the cornea and the back of the AC. Assuming their study was performed in the standing position, we measure a difference of temperature  $\Delta T = 2.03 \text{ K}$  between the AC and the PC, which leads to a maximum velocity of  $u_{\text{max}} \approx 4.02 \times 10^{-4} \text{ m s}^{-1}$ , which is in the same order of magnitude as our results:  $2.76 \times 10^{-4} \text{ m s}^{-1}$ .

## 5 Results and discussion

### 5.1 Impact of the position of the subject

We first examine how different postural orientations—standing, prone, and supine—affect the flow of the AH in the AC. Fig. 7 presents the simulation results for each position, illustrating the flow patterns and pressure distributions.

In the standing position (Fig. 7(a)), gravity significantly influences the flow, resulting in higher velocities and a pronounced downward movement of the aqueous humor. This enhanced flow contributes to the formation of characteristic patterns such as Krukenberg’s spindle and recirculation zones within the AC, consistent with observations in the literature [Abd+21; Wan+16; Mur+23].

In the prone and supine positions (Figs. 7(b) and 7(c)), the flow patterns are altered due to the change in the direction of gravity relative to the eye. In the prone position, the flow moves from the back of the AC towards the cornea, slightly warming the cornea. Conversely, in the supine position, the flow moves from the cornea towards the back of the AC, leading to a slight cooling effect on the cornea. These variations in flow patterns and velocities directly impact the temperature distribution within the eye, as discussed in Section 4.3, and have potential implications for ocular health and treatment strategies [Kin+18; Bha21].

### 5.2 Wall shear stress and its implications in ocular physiology

We further focus on the wall shear stress (WSS), a critical parameter representing the tangential force per unit area exerted by the fluid on the wall due to viscous effects. The insights gained from WSS analysis can inform clinical practices, contributing to personalized medicine, surgical optimization, and improved device design [Yan+22; Fer+18]. Understanding the WSS distribution has significant implications in ocular physiology, including:

- **Drug delivery:** High WSS regions may enhance the mixing and transport of drug particles within the AH, potentially increasing drug absorption rates through ocular tissues, see [Xu+13; Kou16; SZM13]. By identifying these regions, drug delivery systems can be designed to target specific areas within the eye, improving therapeutic outcomes.
- **Surgical procedures:** WSS analysis provides valuable insights for optimizing surgical interventions, [Kud+20; Bas+24]: (i) Design optimization: Knowledge of WSS distributions helps in planning procedures that minimize

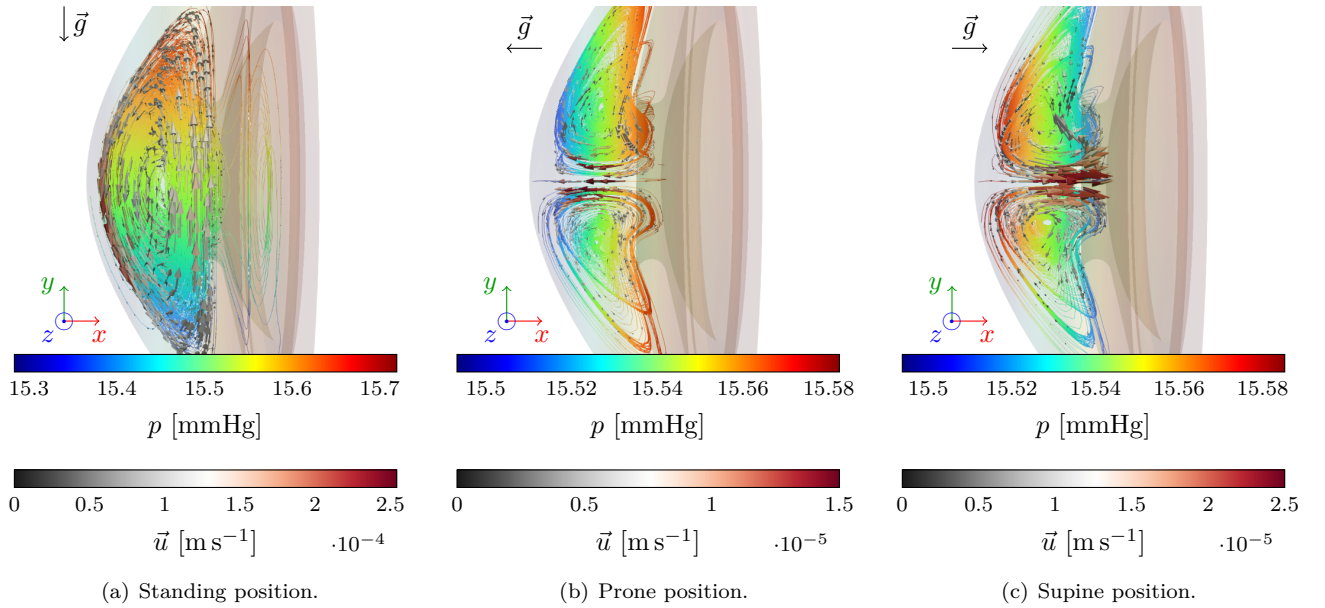


Figure 7: Results of simulation for various postural orientations of the eye. Streamlines are colored according to the pressure, and the arrows show the fluid velocity magnitude.

mechanical stresses on ocular tissues, reducing the risk of tissue damage; *(ii)* Implantable devices: Designing intraocular lenses and drainage devices that account for WSS can help prevent endothelial cell loss and maintain corneal health [Rep+15; Bas+24]; *(iii)* Postoperative outcomes: Monitoring changes in WSS after surgery can help predict healing responses and the risk of complications.

**Definition of Wall Shear Stress** The *wall shear stress*  $\vec{\tau}_w$  at a point on the wall is defined as the magnitude of the tangential component of the stress tensor acting on the wall, and is computed in the present work as:

$$\vec{\tau}_w(\vec{u}, p) = \mu \left. \frac{\partial \vec{u}}{\partial \vec{n}} \right|_{\text{wall}}, \quad (17)$$

under the no-slip boundary condition at the wall. The vector  $\vec{n}$  designates the unit outward normal vector to the wall, and  $\vec{u}_\tau$  is the tangential component of the velocity vector at the wall.

**Numerical considerations** We emphasize that it is difficult to measure WSS experimentally, and numerical simulations are a valuable tool for investigating the complex interactions between the different physical phenomena in the eye, and in particular the WSS distribution, [Kum+06; Yam+10; Qin+21].

However, from a computational standpoint, accurately determining the wall shear stress (WSS) necessitates *(i)* a sufficiently fine mesh resolution near the walls to capture the sharp velocity gradients present in these regions, and *(ii)* a consistent discretization strategy to ensure the accuracy of the computed WSS. To achieve the former, we apply the mesh discretization strategy ensuring the mesh is adequately refined near the boundaries of  $\Omega_{\text{AH}}$ , as depicted in Fig. 8. Therefore, the mesh used in the following simulation is the mesh **Mr5**, described in Table 4. Regarding the latter, the mesh elements at the interfaces between the domain  $\Omega_{\text{AH}}$  and the surrounding tissues exhibit varying normal vectors, the direction of which are not uniformly defined across all elements. Since the velocity field is approximated using a  $\mathbb{P}_2$  finite element space, its gradient is naturally of order 1, but discontinuous. Accordingly, we employ a  $\mathbb{P}_{1,\text{disc}}$  approximation space to compute the WSS, ensuring consistency and accuracy. In addition, we compute a continuous piece-wise linear approximation ( $[L^2]^3$ -projection of the discontinuous approximation) of the WSS to avoid numerical oscillations and improve the visualization of the results.

512.14963pt

**Simulation results** We compute the WSS on the surfaces of the anterior chamber to analyze the shear stresses resulting from the AH flow under different postural orientations. Fig. 9 displays the WSS magnitude over the corneal endothelium for the standing, prone, and supine positions.

We first present in Table 7 a comparative analysis between the magnitude of the WSS obtained in this study and various numerical findings from the literature. Note that some differences in the modeling and computational framework should be accounted for: *(i)* in [Fer+18; Qin+21], an inlet and outlet flow boundary condition was used,

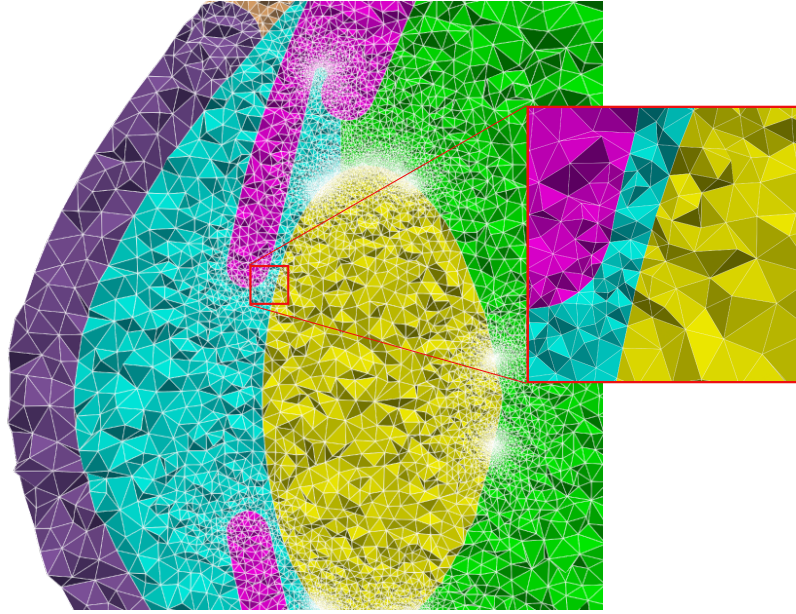
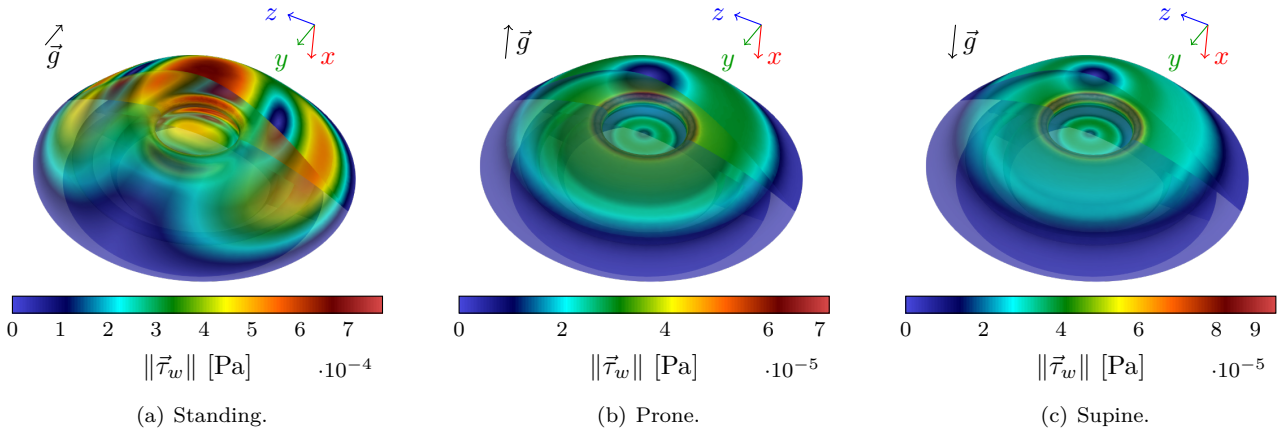
Figure 8: Refinement of mesh Mr3 near the wall boundary of  $\Omega_{AH}$ .

Figure 9: Wall shear stress distribution on the corneal endothelium for the three postural orientations.

(ii) in [Kud+20; Rep+15], the authors imposed an inlet flow and outlet pressure boundary condition. Recall that the model presented in this work uses a no-slip boundary condition on the walls of the anterior chamber.

Despite these differences in boundary conditions, our results show a similar order of magnitude for WSS compared to the literature. The slightly lower values in our model may be attributed to the no-slip condition applied at the walls, which tends to reduce shear stress near the boundaries. Moreover, when comparing the distribution of the WSS, shown in Figs. 9(a) and 9(c), with results presented in [Qin+21, Fig. 5], we observe a similar pattern, with higher values near the corneal endothelium and lower values near the iris and lens surfaces. Furthermore, in [Can+02], the authors reported a theoretically derived value of  $\|\tau_w\| \approx \Delta T \cdot 1.98 \times 10^{-4} \text{ Pa K}^{-1}$ . In the standing position, we find  $\Delta T = 2.03 \text{ K}$ , leading to  $\|\tau_w\| \approx 13.6 \times 10^{-4} \text{ Pa}$ , which is in the same order of magnitude as the maximum WSS values obtained in our simulations:  $\|\tau_w\| \approx 7.7 \times 10^{-4} \text{ Pa}$ .

Building on the sensitivity analysis (SA) presented in our previous work [SPS24], we next examine the effect of ambient temperature on the WSS magnitude. Specifically, we calculate the average WSS magnitude across three surfaces within the anterior chamber as a function of ambient temperature for each of the three postural orientations: (i) on the corneal endothelium, denoted by  $\Gamma_{\text{cornea}}$ , (ii) on the iris surface, denoted by  $\Gamma_{\text{iris}}$ , and (iii) on the entire boundary of the anterior chamber, denoted by  $\partial\Omega_{AH}$ . On the basis of [SPS24], we conduct our analysis for a range of  $T_{\text{amb}}$  of [283, 323] K, with a baseline value of  $T_{\text{amb}} = 294 \text{ K}$ .

The results are presented in Fig. 10. The first striking result is that the WSS magnitude is significantly influenced by the postural orientation or the subject: in horizontal positions (prone and supine), the WSS magnitude is ten times lower than in the standing position. This observation is coherent with the fact that for corneal surgery, after the injection of endothelial cells inside the aqueous humor or the patient, the patient is placed in prone position for three hours to enhance the adhesion of the cells to the cornea [Kin+18].

Reference	Boundary conditions	Orientation	Range of WSS
Fernández-Vigo et al. [Fer+18]	Inlet/outlet flow	n/a	$[10^{-5}, 1.7 \cdot 10^{-3}]$
Kudsieh et al. [Kud+20]	Inlet flow/outlet pressure	n/a	$[0, 1.36 \cdot 10^{-3}]$
Repetto et al. [Rep+15]	Inlet flow/outlet pressure	Standing	$[0, 1.63 \cdot 10^{-3}]$
Qin et al. [Qin+21]	Inlet/outlet flow	Standing Supine	$[5 \cdot 10^{-4}, 3.5 \cdot 10^{-3}]$ $[10^{-4}, 10^{-3}]$
Canning et al. [Can+02]	No-slip velocity	Standing	$[0, 1.36 \cdot 10^{-3}]$
Current model	No-slip velocity	Standing	$[0, 7.7 \cdot 10^{-4}]$
		Supine	$[0, 9.5 \cdot 10^{-5}]$
		Prone	$[0, 7.2 \cdot 10^{-5}]$

Table 7: WSS range (in Pa), for various configurations, comparison with numerical results from the literature.

In addition, the results indicate a complex dependency of the WSS magnitude on ambient temperature. In the three positions, the WSS magnitude reaches a minimum around  $T_{\text{amb}} = 310$  K, corresponding to the body temperature. Such a limitation is further discussed in the next section.

In, our findings show that the WSS magnitude is significantly influenced by both postural orientation and ambient temperature. These factors should be thus considered in the design of ocular devices and drug delivery systems to optimize therapeutic outcomes.

## 6 Conclusion and perspectives

This work presented a comprehensive modeling and computational framework for simulating heat transfer within the human eyeball, coupled with the flow of AH in both the anterior and posterior chambers of a healthy eye. Our complex model has undergone rigorous verification and validation against numerical results from existing literature, demonstrating its accuracy and reliability.

The simulation results showed flow patterns and temperature distributions that align closely with previous numerical studies, reinforcing the validity of our approach. Notably, the model accurately captured the impact of postural orientation on flow recirculations within the eye [Wan+16; Abd+21; Mur+23], providing valuable insights into ocular physiology and the effects of gravity on intraocular fluid dynamics.

Additionally, we have computed the wall shear stress (WSS) distributions within the eye, providing a foundational layer for future applications in drug delivery and surgical planning. Our findings showed good agreement with previously reported results [Fer+18; Kud+20; Rep+15; Qin+21; Can+02]. Moreover, we thoroughly assessed the impact of the postural orientation and of the ambient temperature on the WSS. This analysis is crucial for understanding the mechanical forces acting on ocular tissues, which can influence drug absorption rates, endothelial cell health, and surgical outcomes [Yan+22; Fer+18].

An important novelty of our work lies in the integration of high-performance computing (HPC) techniques to solve the coupled heat transfer on the entire eye geometry, with fluid flow equations in both the anterior and posterior chambers. This holistic approach allows for a more accurate representation of intraocular phenomena compared to models that focus solely on the anterior chamber or neglect the posterior chamber. By leveraging HPC resources efficiently, we can handle the computational demands of such detailed simulations, enabling high-resolution analyses that were previously impractical.

Despite these successes, a primary drawback of the present model is its computational cost, which remains relatively high—requiring several minutes on the specified hardware to perform a single simulation. This computational intensity limits the feasibility of real-time simulations, which are desirable for clinical applications and interactive studies.

To address the computational challenges, we are working on improving the preconditioner for the conjugate heat transfer problem, in particular the Schur complement preconditioner for the fluid block. The challenge is to significantly reduce the computational cost while enable many parameter or real-time evaluations. We are currently developing model order reduction techniques tailored to our problem, extending our previous work [SPS24]. These methods, such as the (certified) reduced basis method [Pru+02], aim to enable real-time simulations of coupled flow and heat transfer inside the human eyeball by reducing the computational complexity while preserving essential dynamics. Implementing such techniques will significantly enhance the model’s applicability in clinical settings, allowing for rapid simulations that can assist in diagnosis and treatment planning.

Another extension of this work involves incorporating AH inflow and outflow mechanisms, which were neglected in the current model under the assumption of minimal influence on overall flow dynamics, as in [NOR08; Kum+06]. Including AH production and drainage would provide a better understanding of intraocular fluid dynamics, especially under pathological conditions such as glaucoma, where these processes are disrupted. This requires modeling AH



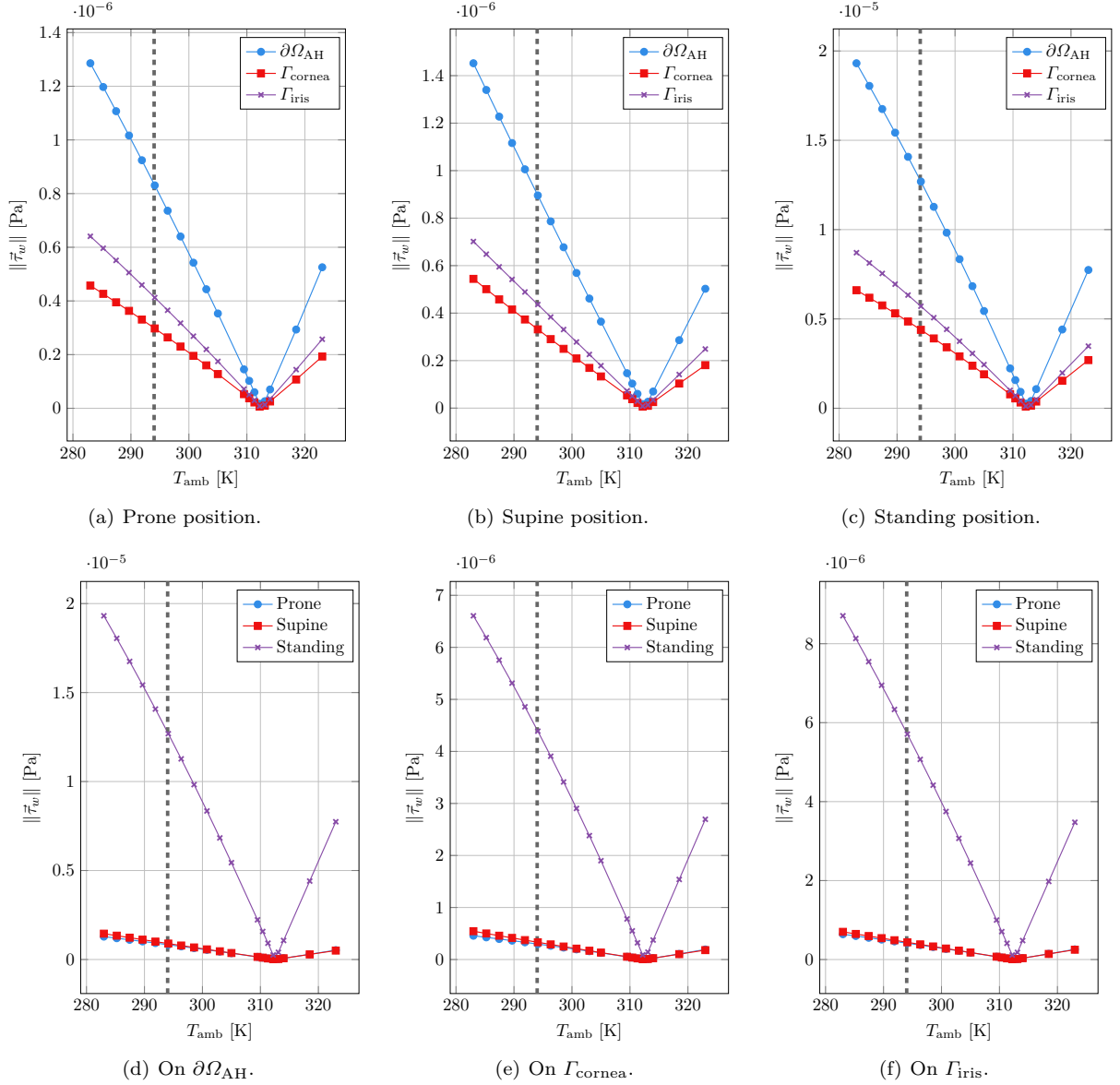


Figure 10: Average of the wall shear stress magnitude as a function of the ambient temperature for the three postural orientations, at different location (top row), and impact of the posture on each specific boundaries (bottom row). The vertical line at  $T_{amb} = 294$  K represents the baseline value as per Table 2.

production in the ciliary body and the trabecular meshwork's drainage function [Dvo+19] using appropriate boundary conditions.

From a clinical perspective, our framework holds significant potential for assessing the effects of topical administration of ophthalmic drugs, such as eye drops [Bha21] or localized hyperthermia treatments [Gon+23]. Additionally, it could be instrumental in evaluating cell injection treatments for internal pathologies, such as bullous keratopathy [Kin+18]. Future research will focus on integrating drug transport models and cell injection into our simulations, enabling the study of diffusion, absorption, and interaction with ocular tissues. This integration will facilitate the development of personalized medicine approaches and improve therapeutic strategies by predicting drug efficacy and optimizing dosing regimens.

In summary, this work lays the foundation for advanced computational modeling of ocular fluid dynamics and heat transfer, with promising applications in both research and clinical practice. The ongoing developments aim to enhance the model's capabilities and usability, bringing us closer to real-time, patient-specific simulations that can inform diagnosis, treatment planning, and potentially device design in ophthalmology.

## Acknowledgments

The authors would like to acknowledge the support of the Cemosis platform at the University of Strasbourg and the French Ministry of Higher Education, Research and Innovation.

Part of this work was also funded by the France 2030 NumPEX Exa-MA (ANR-22-EXNU-0002) project managed by the French National Research Agency (ANR).

## Data availability statement

The geometrical data that support the findings of this study are available in [Cha+24]. All the codes used to run the simulations, as well as the meshed employed in this work, are available in [Sai+24b].

## Material and methods

### Ethical statement

None

## References

- [Li+10] Eric Li et al. “Modeling and simulation of bioheat transfer in the human eye using the 3D alpha finite element method”. In: *International Journal for Numerical Methods in Biomedical Engineering* (Mar. 2010), p. 22. DOI: 10.1002/cnm.1372.
- [Kin+18] Shigeru Kinoshita et al. “Injection of Cultured Cells with a ROCK Inhibitor for Bullous Keratopathy”. In: *New England Journal of Medicine* 378.11 (Mar. 2018), pp. 995–1003. ISSN: 0028-4793, 1533-4406. DOI: 10.1056/NEJMoa1712770. URL: <http://www.nejm.org/doi/10.1056/NEJMoa1712770>.
- [Bha21] Ajay Bhandari. “Ocular Fluid Mechanics and Drug Delivery: A Review of Mathematical and Computational Models”. In: *Pharmaceutical Research* 38.12 (Dec. 2021), pp. 2003–2033. ISSN: 0724-8741, 1573-904X. DOI: 10.1007/s11095-021-03141-6. URL: <https://link.springer.com/10.1007/s11095-021-03141-6>.
- [RF77] Robert F. Rosenbluth and Irving Fatt. “Temperature measurements in the eye”. In: *Experimental Eye Research* 25.4 (Oct. 1977), pp. 325–341. ISSN: 00144835. DOI: 10.1016/0014-4835(77)90100-2. URL: <https://linkinghub.elsevier.com/retrieve/pii/0014483577901002>.
- [Dvo+19] Mariia Dvoriashyna et al. “Mathematical Models of Aqueous Production, Flow and Drainage”. In: *Ocular Fluid Dynamics*. Ed. by Giovanna Guidoboni, Alon Harris, and Riccardo Sacco. Series Title: Modeling and Simulation in Science, Engineering and Technology. Cham: Springer International Publishing, 2019, pp. 227–263. ISBN: 978-3-030-25886-3. DOI: 10.1007/978-3-030-25886-3\_9. URL: [http://link.springer.com/10.1007/978-3-030-25886-3\\_9](http://link.springer.com/10.1007/978-3-030-25886-3_9).
- [HB02] Jeffrey J. Heys and Victor H. Barocas. “A boussinesq model of natural convection in the human eye and the formation of Krukenberg’s spindle”. In: *Annals of Biomedical Engineering* 30.3 (Mar. 2002), pp. 392–401. ISSN: 0090-6964. DOI: 10.1114/1.1477447.
- [Wan+16] Wenjia Wang et al. “Fluid and structure coupling analysis of the interaction between aqueous humor and iris”. In: *BioMedical Engineering OnLine* 15.S2 (Dec. 2016), p. 133. ISSN: 1475-925X. DOI: 10.1186/s12938-016-0261-3. URL: <http://biomedical-engineering-online.biomedcentral.com/articles/10.1186/s12938-016-0261-3>.
- [Mur+23] Javier Murgoitio-Esandi et al. “A Mechanistic Model of Aqueous Humor Flow to Study Effects of Angle Closure on Intraocular Pressure”. In: *Translational Vision Science & Technology* 12.1 (Jan. 2023), p. 16. ISSN: 2164-2591. DOI: 10.1167/tvst.12.1.16. URL: <https://doi.org/10.1167/tvst.12.1.16>.
- [Sac+23] Riccardo Sacco et al. “The role of conventional and unconventional adaptive routes in lowering of intraocular pressure: Theoretical model and simulation”. In: *Physics of Fluids* 35.6 (June 2023), p. 061902. ISSN: 1070-6631, 1089-7666. DOI: 10.1063/5.0151091. URL: <https://pubs.aip.org/pof/article/35/6/061902/2895206/The-role-of-conventional-and-unconventional>.
- [Can+02] C. R. Canning et al. “Fluid flow in the anterior chamber of a human eye”. In: *IMA journal of mathematics applied in medicine and biology* 19.1 (Mar. 2002), pp. 31–60. ISSN: 0265-0746.
- [ON08] Ean-Hin Ooi and Eddie Yin-Kwee Ng. “Simulation of aqueous humor hydrodynamics in human eye heat transfer”. In: *Computers in Biology and Medicine* 38.2 (Feb. 2008), pp. 252–262. ISSN: 00104825. DOI: 10.1016/j.combiomed.2007.10.007. URL: <https://linkinghub.elsevier.com/retrieve/pii/S001048250700176X>.

- [BBS20] Ajay Bhandari, Ankit Bansal, and Niraj Sinha. “Effect of aging on heat transfer, fluid flow and drug transport in anterior human eye: A computational study”. In: *Journal of Controlled Release* 328 (Dec. 2020), pp. 286–303. ISSN: 01683659. DOI: 10.1016/j.jconrel.2020.08.044. URL: <https://linkinghub.elsevier.com/retrieve/pii/S0168365920304855>.
- [Abd+21] Farah Abdelhafid et al. “Operator Splitting for the Simulation of Aqueous Humor Thermo-Fluid-Dynamics in the Anterior Chamber”. In: *Recent Developments in Mathematical, Statistical and Computational Sciences*. Ed. by D. Marc Kilgour et al. Vol. 343. Series Title: Springer Proceedings in Mathematics & Statistics. Cham: Springer International Publishing, 2021, pp. 489–499. ISBN: 978-3-030-63590-9. DOI: 10.1007/978-3-030-63591-6\_45. URL: [https://link.springer.com/10.1007/978-3-030-63591-6\\_45](https://link.springer.com/10.1007/978-3-030-63591-6_45).
- [Dvo+22] Mariia Dvoriashyna et al. “A Mathematical Model of Aqueous Humor Production and Composition”. In: *Investigative Ophthalmology & Visual Science* 63.9 (Aug. 2022), p. 1. ISSN: 1552-5783. DOI: 10.1167/iovs.63.9.1. URL: <https://iovs.arvojournals.org/article.aspx?articleid=2783533>.
- [SPS24] Thomas Saigre, Christophe Prud’homme, and Marcela Szopos. “Model order reduction and sensitivity analysis for complex heat transfer simulations inside the human eyeball”. In: *International Journal for Numerical Methods in Biomedical Engineering* 40.11 (Sept. 2024), e3864. ISSN: 2040-7939, 2040-7947. DOI: 10.1002/cnm.3864. URL: <https://onlinelibrary.wiley.com/doi/10.1002/cnm.3864>.
- [Sai+24a] Thomas Saigre et al. “A coupled fluid-dynamics-heat transfer model for 3D simulations of the aqueous humor flow in the human eye”. In: *8th International Conference on Computational and Mathematical Biomedical Engineering – CMBE2024 Proceedings*. Vol. 2. Arlington (Virginia), United States: P. Nithiarasu and R. Löhner (Eds.), June 2024, pp. 508–512. ISBN: 978-0-9562914-7-9. URL: <https://hal.science/hal-04558924>.
- [Yan+22] Shu Yang et al. “Unraveling the mechanobiology of cornea: From bench side to the clinic”. In: *Frontiers in Bioengineering and Biotechnology* 10 (Oct. 2022), p. 953590. ISSN: 2296-4185. DOI: 10.3389/fbioe.2022.953590. URL: <https://www.frontiersin.org/articles/10.3389/fbioe.2022.953590/full>.
- [ESW14] Howard C. Elman, David J. Silvester, and Andrew J. Wathen. *Finite elements and fast iterative solvers: with applications in incompressible fluid dynamics*. 2. ed. Numerical mathematics and scientific computation. Oxford: Oxford Univ. Press, 2014. ISBN: 978-0-19-967879-2.
- [Sai24] Thomas Saigre. “Mathematical modeling, simulation and reduced order modeling of ocular flows and their interactions: Building the Eye’s Digital Twin”. Theses. Université de Strasbourg, Dec. 2024. URL: <https://theses.hal.science/tel-04813671>.
- [Cha+24] Vincent Chabannes et al. *A 3D geometrical model and meshing procedures for the human eyeball*. Sept. 2024. DOI: 10.5281/ZENODO.13829740. URL: <https://zenodo.org/doi/10.5281/zenodo.13829740>.
- [Sai+24b] Thomas Saigre et al. *Mesh and configuration files to perform coupled heat+fluid simulations on a realistic human eyeball geometry with Feel++*. Oct. 2024. DOI: 10.5281/ZENODO.13886143. URL: <https://zenodo.org/doi/10.5281/zenodo.13886143>.
- [Dvo+18] M Dvoriashyna et al. “Aqueous humour flow in the posterior chamber of the eye and its modifications due to pupillary block and iridotomy”. In: *Mathematical Medicine and Biology: A Journal of the IMA* 35.4 (Dec. 2018), pp. 447–467. ISSN: 1477-8599, 1477-8602. DOI: 10.1093/imammb/dqx012. URL: <https://academic.oup.com/imammb/article/35/4/447/4582768>.
- [RRK13] R Ramakrishnan, Shalmali Ranaut, and Mona Khurana. “Aqueous Humor Dynamics”. In: *Diagnosis and Management of Glaucoma*. Jaypee Brothers Medical Publishers (P) Ltd., 2013, pp. 76–76. ISBN: 978-93-5025-578-0. DOI: 10.5005/jp/books/11801\_9. URL: <https://www.jaypeedigital.com/book/9789350255780/chapter/ch9>.
- [NO06] E.Y.K. Ng and E.H. Ooi. “FEM simulation of the eye structure with bioheat analysis”. In: *Computer Methods and Programs in Biomedicine* 82.3 (June 2006), pp. 268–276. ISSN: 01692607. DOI: 10.1016/j.cmpb.2006.04.001. URL: <https://linkinghub.elsevier.com/retrieve/pii/S0169260706000708>.
- [DR04] P. G. Drazin and W. H. Reid. *Hydrodynamic Stability*. 2nd ed. Cambridge University Press, Aug. 2004. ISBN: 978-0-521-52541-1 978-0-511-61693-8. DOI: 10.1017/CB09780511616938. URL: <https://www.cambridge.org/core/product/identifier/9780511616938/type/book>.
- [Kum+06] Satish Kumar et al. “Numerical Solution of Ocular Fluid Dynamics in a Rabbit Eye: Parametric Effects”. In: *Annals of Biomedical Engineering* 34.3 (Mar. 2006), pp. 530–544. ISSN: 0090-6964, 1573-9686. DOI: 10.1007/s10439-005-9048-6. URL: <http://link.springer.com/10.1007/s10439-005-9048-6>.
- [Tsu15] Yutaka Tsuzuki. “Existence and Uniqueness of Solutions to Heat Equations with Hysteresis Coupled with Navier–Stokes Equations in 2D and 3D”. In: *Journal of Mathematical Fluid Mechanics* 17.3 (Sept. 2015), pp. 577–597. ISSN: 1422-6928, 1422-6952. DOI: 10.1007/s00021-015-0210-0. URL: <http://link.springer.com/10.1007/s00021-015-0210-0>.

- [CAS22] Open CASCADE. *SALOME: The Open Source Integration Platform for Numerical Simulation*. 2022. URL: <https://salome-project.org>.
- [MMG22] MMG tools. *MMG: a mesh-based finite element library*. 2022. URL: <https://www.mmgtools.org/>.
- [Pru+24] Christophe Prud'homme et al. *feelpp/feelpp: Feel++ Release V111 preview.10*. July 2024. DOI: 10.5281/ZENODO.12742155. URL: <https://zenodo.org/doi/10.5281/zenodo.12742155>.
- [Bal+24] Satish Balay et al. *PETSc Web page*. 2024. URL: <https://petsc.org/>.
- [Sco88] J A Scott. "A finite element model of heat transport in the human eye". In: *Physics in Medicine and Biology* 33.2 (Feb. 1988), pp. 227–242. ISSN: 0031-9155, 1361-6560. DOI: 10.1088/0031-9155/33/2/003. URL: <https://iopscience.iop.org/article/10.1088/0031-9155/33/2/003>.
- [KS10] Andreas Karampatzakis and Theodoros Samaras. "Numerical model of heat transfer in the human eye with consideration of fluid dynamics of the aqueous humour". In: *Physics in Medicine and Biology* 55.19 (Oct. 2010), pp. 5653–5665. ISSN: 0031-9155, 1361-6560. DOI: 10.1088/0031-9155/55/19/003. URL: <https://iopscience.iop.org/article/10.1088/0031-9155/55/19/003>.
- [EYB89] N. Efron, G. Young, and N. A. Brennan. "Ocular surface temperature". In: *Current Eye Research* 8.9 (Sept. 1989), pp. 901–906. ISSN: 0271-3683.
- [Fer+18] José Ignacio Fernández-Vigo et al. "Computational simulation of aqueous humour dynamics in the presence of a posterior-chamber versus iris-fixed phakic intraocular lens". In: *PLOS ONE* 13.8 (Aug. 2018). Ed. by Paloma B. Liton, e0202128. ISSN: 1932-6203. DOI: 10.1371/journal.pone.0202128. URL: <https://dx.plos.org/10.1371/journal.pone.0202128>.
- [Xu+13] Yingqian Xu et al. "A potential model for drug screening by simulating the effect of shear stress in vivo on endothelium". In: *Biorheology* 50.1-2 (2013), pp. 33–43. ISSN: 0006355X. DOI: 10.3233/BIR-130624. URL: <https://www.medra.org/servlet/aliasResolver?alias=iospress&doi=10.3233/BIR-130624>.
- [Kou16] Aristotle G. Koutsiaris. "Wall shear stress in the human eye microcirculation in vivo, segmental heterogeneity and performance of in vitro cerebrovascular models". In: *Clinical Hemorheology and Microcirculation* 63.1 (July 2016), pp. 15–33. ISSN: 13860291, 18758622. DOI: 10.3233/CH-151976. URL: <https://www.medra.org/servlet/aliasResolver?alias=iospress&doi=10.3233/CH-151976>.
- [SZM13] Till Saxer, Andreas Zumbuehl, and Bert Müller. "The use of shear stress for targeted drug delivery". In: *Cardiovascular Research* 99.2 (July 2013), pp. 328–333. ISSN: 1755-3245, 0008-6363. DOI: 10.1093/cvr/cvt102. URL: <https://academic.oup.com/cardiovasres/article-lookup/doi/10.1093/cvr/cvt102>.
- [Kud+20] Bachar Kudsieh et al. "Numerical model to predict and compare the hypotensive efficacy and safety of minimally invasive glaucoma surgery devices". In: *PLOS ONE* 15.9 (Sept. 2020). Ed. by Ahmed Awadein, e0239324. ISSN: 1932-6203. DOI: 10.1371/journal.pone.0239324. URL: <https://dx.plos.org/10.1371/journal.pone.0239324>.
- [Bas+24] Nicol Basson et al. "A computational fluid dynamics investigation of endothelial cell damage from glaucoma drainage devices". In: *Scientific Reports* 14.1 (Feb. 2024), p. 3777. ISSN: 2045-2322. DOI: 10.1038/s41598-023-50491-9. URL: <https://www.nature.com/articles/s41598-023-50491-9>.
- [Rep+15] Rodolfo Repetto et al. "Phakic Iris-Fixated Intraocular Lens Placement in the Anterior Chamber: Effects on Aqueous Flow". In: *Investigative Ophthalmology & Visual Science* 56.5 (May 2015), p. 3061. ISSN: 1552-5783. DOI: 10.1167/iovs.14-16118. URL: <http://iovs.arvojournals.org/article.aspx?doi=10.1167/iovs.14-16118>.
- [Yam+10] Yasuaki Yamamoto et al. "Effect of Anterior Chamber Depth on Shear Stress Exerted on Corneal Endothelial Cells by Altered Aqueous Flow after Laser Iridotomy". In: *Investigative Ophthalmology & Visual Science* 51.4 (Apr. 2010), p. 1956. ISSN: 1552-5783. DOI: 10.1167/iovs.09-4280. URL: <http://iovs.arvojournals.org/article.aspx?doi=10.1167/iovs.09-4280>.
- [Qin+21] Zhangrong Qin et al. "Aqueous humor dynamics in human eye: A lattice Boltzmann study". In: *Mathematical Biosciences and Engineering* 18.5 (2021), pp. 5006–5028. ISSN: 1551-0018. DOI: 10.3934/mbe.2021255. URL: <http://www.aimspress.com/article/doi/10.3934/mbe.2021255>.
- [Pru+02] C. Prud'homme et al. "Reliable Real-Time Solution of Parametrized Partial Differential Equations: Reduced-Basis Output Bound Methods". In: *Journal of Fluids Engineering* 124.1 (Mar. 2002), pp. 70–80. ISSN: 0098-2202, 1528-901X. DOI: 10.1115/1.1448332. URL: <https://asmedigitalcollection.asme.org/fluidsengineering/article/124/1/70/462808/Reliable-RealTime-Solution-of-Parametrized-Partial>.

- [NOR08] Eddie-Yin-Kwee Ng, Ean-Hin Ooi, and U. Rajendra Archarya. “A comparative study between the two-dimensional and three-dimensional human eye models”. In: *Mathematical and Computer Modelling* 48.5-6 (Sept. 2008), pp. 712–720. ISSN: 08957177. DOI: 10.1016/j.mcm.2007.11.011. URL: <https://linkinghub.elsevier.com/retrieve/pii/S0895717707003548> (visited on 09/25/2024).
- [Gon+23] D. Gongal et al. “Thermal finite element analysis of localized hypothermia treatment of the human eye”. In: *Medical Engineering & Physics* 111 (Jan. 2023), p. 103928. ISSN: 13504533. DOI: 10.1016/j.medengphy.2022.103928. URL: <https://linkinghub.elsevier.com/retrieve/pii/S135045332200176X>.